POLITECNICO DI TORINO

Master degree course in Nanotechnologies for ICTs

Master Degree Thesis

Optimal design, fabrication and characterization of fullerene-free, large scale organic solar cells using roll-processing

Supervisor
Prof. Elena Maria Tresso

Candidate
Eva Mazzolini

Co-supervisors
Prof. Jens Wenzel Andreasen
Dr. Moises Espindola Rodriguez
Marcial Fernández Castro

A.A. 2019-2020

Summary

The Sun can provide us with a virtually infinite amount of energy, and this is why solar cells represent one of the leading technologies for renewable energy harvesting. Among those, organic photovoltaics (OPVs) have the benefit of short energy payback times and high manufacturing speeds using large-scale roll-to-roll processing at ambient temperatures. However, they are not yet competitive on the market due to their insufficient stability and efficiency, but recent progress on non-fullerene acceptor materials has made it possible to overcome the 15% PCE mark in lab-scale devices.

The aim of the project is to obtain a device with the highest possible efficiency using only scalable techniques. This is done by optimizing the chosen active layer, hole transport layer and back electrode depositions on top of a flexible substrate. The main fabrication techniques used are slot-die coating, thermal evaporation and flexographic printing.

The study of the optimal active layer is conducted on a system based on a combination of a polymer, P3HT, and a small molecule, O-IDTBR. Our study is conducted by varying the solvents of the active layer solution, the temperature of the bed and the slot-die head during the deposition, and the thickness through the coating parameters (speed and flow rate). The hole transport layer study will be focused on PEDOT:PSS of different viscosities, varying the thickness of the layer. Finally, Ag, Cu and Au are tested for electrode purposes and compared to cheaper, open-air printed Silver paste, as well as different techniques for their deposition. Characterization of the final devices includes testing under a Sun simulator, EQE and transmittance measurements, as well as electrical characterization. The study is enriched with AFM images to get insight on the nanostructure of the active layer.

Contents

List of Tables

List of Figures

Chapter 1

Introduction

As the planet faces an environmental crisis, around 80% of the world's energy is still supplied by fossil fuels. [1] Amongst these are coal, petroleum and natural gas. Nuclear energy makes up around 3% of the total energy supply, and albeit non-fossil, Uranium is still a finite resource. Alarmingly, only around 15% of energy is supplied by renewable sources, with biomass making up most of it at 12%. If no changes in energy distribution are made, the oil and coal supplies will be depleted within 50 years [2]. This, combined with the problem of global warming, is why focusing on the use of renewable energy technologies is paramount in this day and age. Renewable sources, as the word suggests, are those that do not run out in time, and include wind power, tidal, biomass and solar radiation, amongst others. Unfortunately, in 2018, solar energy only accounted for approximately 0.2% of the world energy supply. This is especially ironic when we consider available energy: currently, the global energy demand is over 15 TW, and direct radiation can deliver approximately 26,000 TW. This is possibly the main argument in favour of photovoltaics, yet they are not the leading renewable technology on the market to this day, even though the first solar cells were built around the same time as the first fossil-fueled plants, in the 1880s.

The main photovoltaic technology on the market is undoubtedly Silicon. This stems from many reasons: since the discovery that Silicon produced a greater photovoltaic effect than Selenium, around the same time the transistor was invented, research has been focused on Si. The discovery of the p-n junction revolutionized the way that photovoltaics were seen, and the first Si solar

cells were soon used in space applications. Considering the absolute dominance of Si in the technological industry, it is easy to see why researchers would want to develop a type of photovoltaics that could be fabricated with the same Si wafer processes as other existing devices.
Silicon is also used in its amorphous form in thin film photovoltaic cells, where very thin layers of material are deposited onto different substrates such as glass, plastic, etc. These find their applications mainly in building-integrated photovoltaics and solar farms.

In the past few years, a new technological wave has revolutionized the world of photovoltaics: third generation solar cells. Amongst these, we can find dye-synthesized solar cells, perovskite solar cells and organic solar cells, the latter being the protagonists of this project.

Organic solar cells, also called OPV or OSC, have the benefit of short energy payback time (EPBT) [3], which is defined as the time needed by the device to produce as much energy as the amount used during its production. Additionally, they have low costs compared to other technologies due to the nature of the materials used for their production. They can be flexible, light weight, and rare-earth free, and can be produced in large scale thanks to manufacturing processes such as roll-to-roll and sheet-to-sheet. [4].

As of today, OPVs have not found their way into commercialization due to their poor stabilities and efficiencies. Generally, both can be improved by optimizing the active layer of the organic solar cell, which is made of a donor and an acceptor material.
In the recent years, fullerene derivatives have been extensively researched and used as acceptors in the solar cell stack, however researchers have been able to significantly increase the efficiencies of OPVs with non-fullerene acceptors (NFA), a novel group of materials.
While research on OPV is promising, it is fundamental for OPVs to obtain higher efficiencies and stabilities in order to aim for commercialization. Another fundamental aspect is the scalability of this technology, which is often overlooked in favour of efficiency progress. This issue will be extensively discussed in this work, which aims at fabricating flexible, ITO and fullerene-free OPVs using only scalable techniques, in an effort to step forward towards the goal of commercialization.

Chapter 2

Theoretical background

The first time a photovoltaic effect was witnessed in an organic material dates back to 1959, when Kallmann et al. measured an external voltage on a single crystal of anthracene under illumination. [5]
This effect is now used to produce solar cells that are flexible, lightweight, and low cost. This chapter will give a brief summary on the principle of conduction in organic semiconductors, it will then illustrate the structure and operation of an OPV, and will end with the characterization techniques that are necessary to assess the performance of one of these cells.

2.1 Conduction in organic semiconductors

Organic electronics have been around since the 1980s, when Koezuka et. al. presented the first OFET based on polythiophene [6]. Organic semiconductors are essential for technologies such as OPVs and OLEDs, and this category of materials includes conjugated polymers, small molecules, and oligomers.
Differently from their inorganic counterparts, which constitute the majority of what we know as electronic devices today, organic semiconductors don't have a valence and conduction band, but their delocalized states create two energy levels that have an analogue meaning.
The equivalent concepts to valence and conduction band in organic semiconductors are the HOMO (highest occupied molecular orbital) and LUMO (lowest unoccupied molecular orbital) levels, respectively. When an organic semiconductor absorbs a photon, an electron-hole pair is formed, called exciton. This pair is held together by Coulomb forces, and conduction requires

the separation of the electron from the hole. This is the main difference between conduction in organic and inorganic semiconductors, and is the reason why dissociation-inducing interfaces are needed in organic devices.

2.2 OPV structure and operation

In OPVs, the exciton separation is done by using a blend of a donor and an acceptor material. The latter has a lower LUMO level than the donor, which will attract electrons to make the dissociation happen.
The operation of these devices can be summarized in 5 steps:

- **Photon absorption:** upon illumination, a photon is absorbed by the active layer
- **Exciton creation:** the bound electron-hole pair is formed
- **Exciton diffusion:** the pair travels in the bulk heterojuction until it reaches a donor/acceptor boundary
- **Charge separation:** the charges are separated. The holes move in the donor material, the electrons in the acceptor material
- **Charge transport:** the now free charges are able to travel through the blend to reach the electrodes.

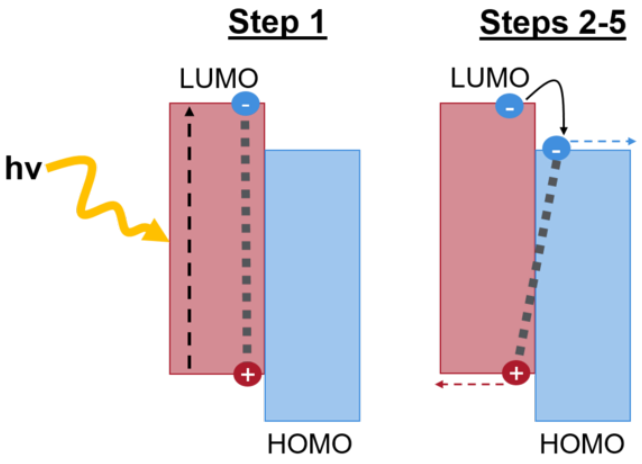

Figure 2.1. Working steps of an OPV in terms of energy levels (red = donor, blue = acceptor) [7]

To understand the functioning of a cell as a whole, each individual layer of an OPV must be introduced.

Substrate

The substrate is the base for the device, and is usually made of PET for flexible devices, but can also be glass (usually in lab-scale devices), or other materials such as textiles [8]. This material determines the type of processing the cells can go through; a flexible substrate such as PET can undergo roll-processing and is therefore adaptable to roll-to-roll processing, while glass is mostly used for spin-coating and other processes used for small-scale devices. Glass can also be used in large modules using, for instance, sheet-to-sheet processing, but flexibility is one of the strengths of this technology, so plastic is preferred. Usually, glass substrates use ITO (Indium Tin Oxide) as their transparent electrode, while plastic substrates can make use of both ITO and printed electrodes. The scarcity of Indium, however, has motivated the use of other materials such as thin layers of PEDOT:PSS enhanced with silver grids [9].

Active layer

This is the most important layer of the whole organic solar cell stack. It is composed of a donor and an acceptor material, which are usually a conjugated polymer and a small molecule respectively, in a configuration such as a single juction, a bulk heterojuction, or more complex structures (Figure 2.2).
Upon illumination, an exciton is formed in the blend, and the high electron affinity of the acceptor material allows for the electron and hole to separate at the D/A interface, to reach the electrodes in opposite directions, creating a charge flow.
Excitons have a short lifetime, and if the donor/acceptor interfaces are close (10-20 nm), there is a chance of separating the electron from the hole without them recombining. This is one of the main arguments in favour of using a bulk heterojunction. Additionally, the processing methods for OPV bulk heterojuctions are simple, as they only require mixing the two materials to form an ink to use for coating. The possibility of solution-processing is one of the main advantages of this technology.

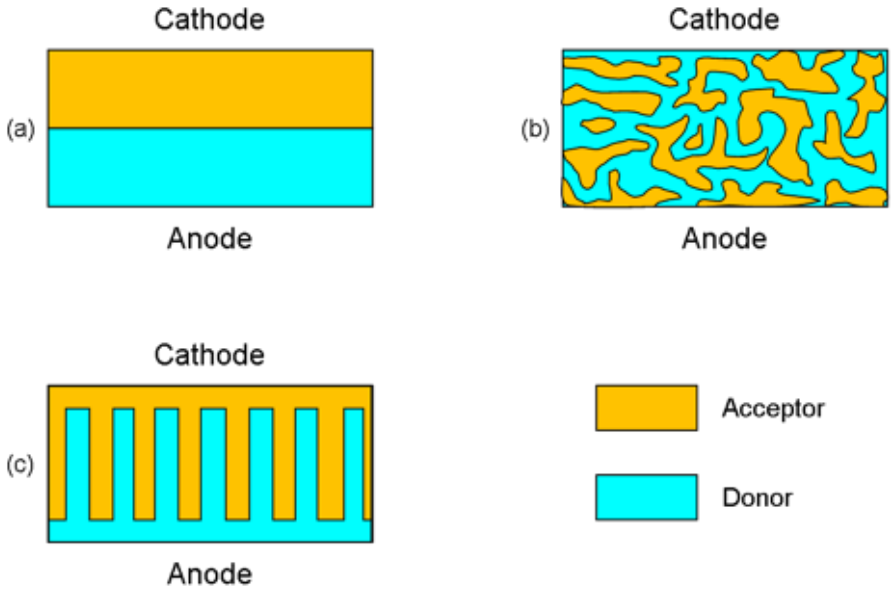

Figure 2.2. Different types of heterojuctions for OPVs [10]

Transport layers: ETL & HTL

Transport layers have the role of directing charge carriers towards a certain electrode. What defines whether a material will be a hole or an electron transport layer is the position of its energy levels compared to the active layer materials. ETL materials include ZnO and TiO, while some common HTLs are PEDOT:PSS and MoOx.

Electrodes

Electrodes have the important role of conducting the charge carriers towards the external circuit. Carriers reach the electrodes thanks to the internal field that is formed when two materials with different energy levels are used as contacts.
The ideal electrode needs to have very low sheet resistance, high selectivity (hole or electron) and must be surface passivating [11]. The materials used are usually metals, and can be physically evaporated, sputtered, printed, etc., but carbon-based and polymer electrodes have also been investigated [12], amongst others.
The electrode that is closest to the substrate is semitransparent to allow the light to enter the device (Figure 2.3).

Geometries

Generally speaking, there are two configurations possible for organic solar cells: a normal one, and an inverted one (Figure 2.3)

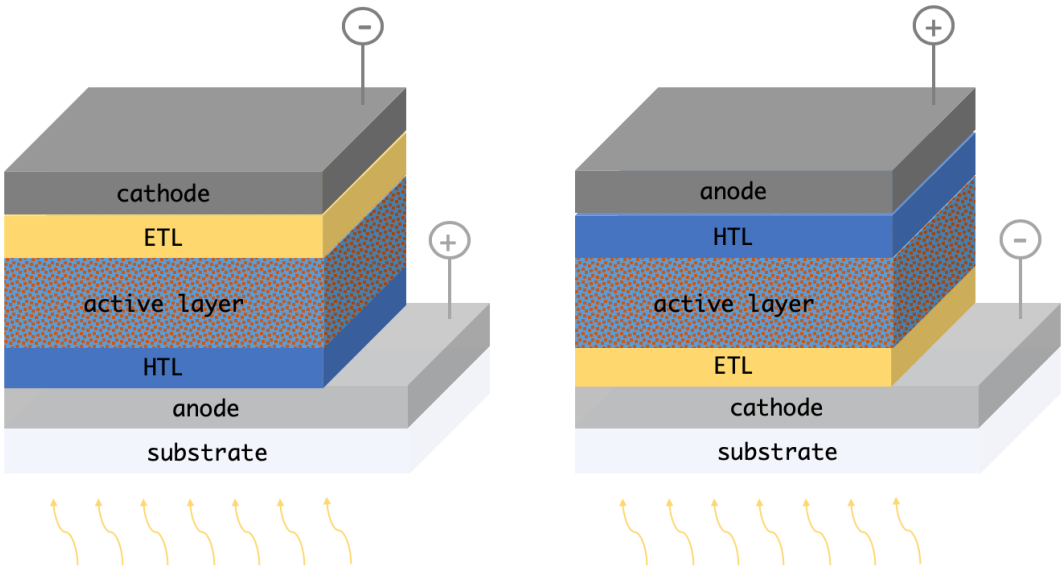

Figure 2.3. Normal (left) and inverted (right) geometries

The working principle is the same in both configurations, the difference lays in the direction of charge flow.

- In normal geometry, the substrate and the transparent electrode are on the side of the positive electrode

- In inverted geometry, the transparent electrode becomes the negative electrode

It is generally easier to fabricate an inverted-geometry OSC, due to the fact that the HTL should be transparent and robust. The most frequently used HTL materials (PEDOT:PSS or metal oxides) cannot fulfill these requirements, but ETL materials do not pose such problems [13]. Moreover, stability is increased in an inverted geomety [14].

2.3 Characterizing OPVs

Solar spectrum and energy

The Sun's spectral irradiance (power density at a given wavelength) is similar to that of a black body, when no atmosphere is taken into consideration. However, the shape of the spectrum that reaches the Earth's surface is different, due to scattering and absorption in the atmosphere. The Air Mass (AM) is a measure of how far solar radiation has to travel to reach the Earth's surface (Figure 2.4):

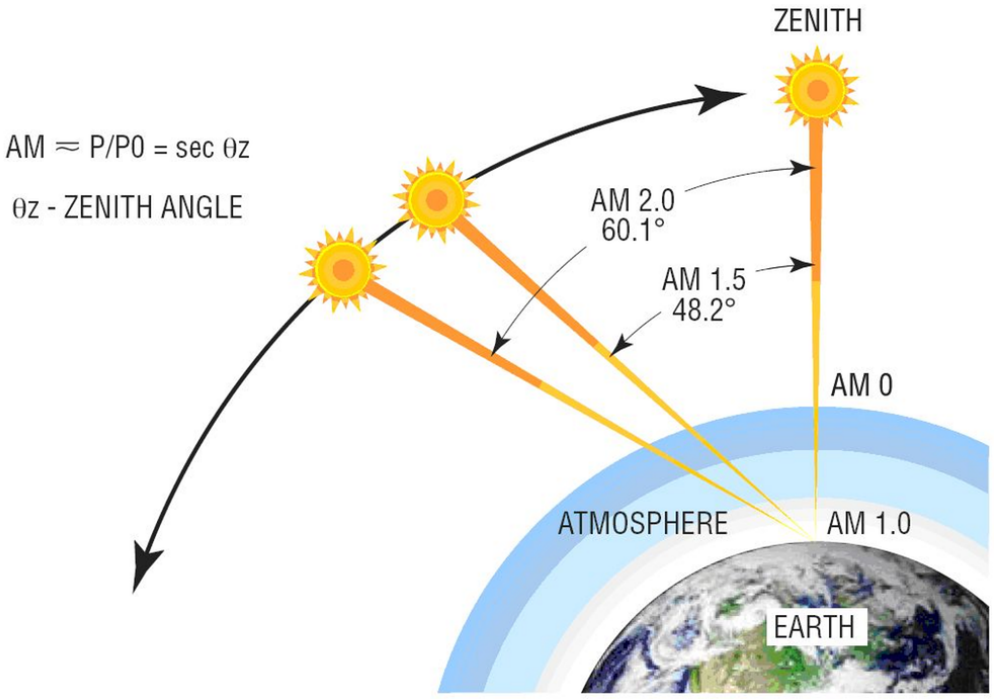

Figure 2.4. Air Mass definitions [15]

Solar simulators

A solar simulator is an instrument that is able to reproduce the illumination conditions of natural sunlight. It is used to test the performance of solar cells, solar screens, and other devices [16]. Usually, for solar cell testing in solar simulators, the AM 1.5G spectrum is used (where the "G" stands for global, and means that the spectrum includes both direct and diffuse radiation), along with an intensity of 1000 W/m^2.

Photovoltaic parameters

Characterization of the photovoltaic parameters of a solar cell is done using a solar simulator, which extracts the current-voltage curves (I-V curves). Such parameters are:

- I_{SC}: this is the current measured when the circuit is in short circuit. It is found as the intersection between the IV curve and the y-axis. In this point, the voltage is zero.
- V_{OC}: this is the voltage measured when the circuit is in open circuit. It is found as the intersection between the IV curve and the x-axis. In this point, the current is zero.
- **Maximum power output** P_{MPP}: this value, which represents the maximum power the solar cell can produce, is not given by the product of V_{OC} and I_{SC}. It can be seen graphically (Figure 2.5):
  It is the product of the current and voltage values corresponding to the

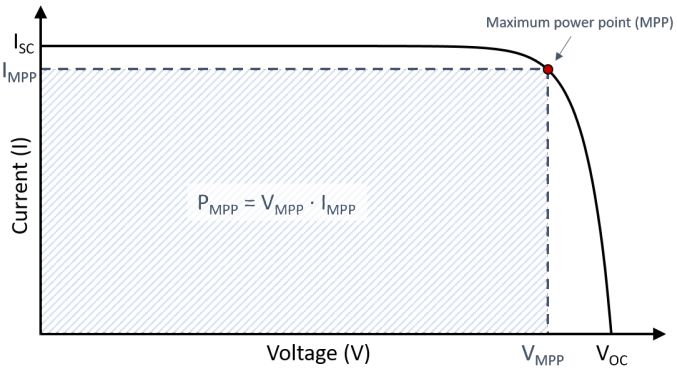

Figure 2.5. IV curve and main parameters [17]

maximum power point (MPP) on the IV curve:

$$P_{MPP} = V_{MPP}.I_{MPP} \tag{2.1}$$

- **Fill factor (FF)**: this represents how close the IV curve is to the ideal situation in which $I_{MPP} = I_{SC}$ and $V_{MPP} = V_{OC}$, or more simply, the area of the rectangle that fills the I-V curve with sides lengths I_{MPP} and V_{MPP} (Figure 2.5. It is computed as:

$$FF = \frac{P_{MPP}}{V_{OC}.I_{SC}} \tag{2.2}$$

- **Power conversion efficiency (PCE or η)**: this is a measure of the generated output power over the input power, and can be computed as:

$$\eta = \frac{P_{out}}{P_{in}} = \frac{V_{OC}.I_{SC}.FF}{P_{in}} \tag{2.3}$$

NB. The J-V (current density-voltage) curves can also be used, as well as J_{sc} (short circuit current density). Using the current density allows to directly compare devices with different areas. These will be used here instead of the current.

Optical characterization

Understanding what part of the electromagnetic spectrum is absorbed by the materials inside a solar cell is fundamental for an efficient device. This is the principle of absorbance spectroscopy. This can be done using a spectrophotometer, a device which exposes the sample to a sequence of wavelengths and measures the amount of absorbed photons.
Another interesting parameter is the transmittance, which can be measured with the same equipment, and shows the portion of the spectrum where the material transmits.

Absorption and transmittance are related by the Lambert-Beer law:

$$T = 10^{-A} \tag{2.4}$$

where T is the transmittance, and A the absorbance.

Optoelectrical characterization

The external quantum efficiency (EQE) of a solar cell is defined as the ratio of collected carriers to the number of photons of a given energy shining outside the cell. Naturally, the EQE depends on the absorption spectrum of the cell, as it practically shows what energies are absorbed and how many of the corresponding charge carriers are collected. The EQE, on top of being a measure of efficiency, can give an insight on how different materials contribute to charge flow, depending on their absorption.

Active layer morphology characterization

As previously mentioned, the morphology of the active layer strongly influences the performance of the solar cell. Imaging the films can be beneficial

to understand whether the fabrication conditions are yielding an optimal or suboptimal morphology and crystallinity. This can be done, for instance, with an Atomic Force Microscope, or with X-Rays. The former yields surface images, while the latter can give information about deeper structures.

Chapter 3

State of the art

Organic photovoltaics have come a long way since their birth. To this day, the record power conversion efficiency for lab-scale devices is set to 17.3% [18]. However, that number is still far from attainable for larger cells, which today hold a record PCE of 11.2% for areas of $1cm^2$ [19]. In this section, we will review the most common fabrication techniques used for film formation, the rise of non-fullerene acceptors, current research on our active layer blend of P3HT:O-IDTBR, and the issues that need to be addressed to move towards the commercialization of these devices.

3.1 Fabrication techniques and scalability

The possibility of being solution-processed onto flexible substrates in the form of inks is definitely one of the strongest arguments in favour OPVs, and it allows for a multitude of manufacturing techniques to be used. More specifically, in order to meet the goal of large scale devices, high throughput fabrication techniques such as roll-to-roll (R2R) must be prioritized, but up-scaling the current high-efficiency systems is not straightforward. In fact, there is a scalability lag that needs to be addressed [20]. This is, on one side, due to the fabrication techniques used for champion, lab-scale devices, which will be discussed in this section; on the other side, some materials making up the solar cell stack cannot undergo processing on flexible substrates such as roll-coating [21].
One step towards this objective is to focus research on systems that can be successfully be roll-processed, in a way that can be compatible with a fully R2R equipment.

Gertsen et. al. have proposed a rigorous classification of deposition methods, considering the continuity of the process, the waste produced, and the amount of cells that it can yield. This section will be a simple overview of the most common fabrication methods currently used for the fabrication of OPVs, and whether they are scalable following the guidelines of ref. [13]. These methods can be separated into three categories: coating, printing and deposition techniques that require vacuum, such as sputtering and thermal evaporation.

Coating

This category includes all of the methods that allow to obtain a wet film with no contact between the substrate and the coating head. Coating techniques allow for very good control of the thickness, but no patterns can be created on the substrate [22]. There are three main techniques used for OPVs within this category: spin-coating, blade coating, and slot-die coating [23].

- **Spin coating** consists of rotating the substrate while the ink is supplied from above, resulting in very thin and uniform films. The downside to this technique is its incompatibility with roll-processing, making it exclusive to lab-scale devices.

- **Blade coating/doctor blading** is a technique that is often used as an intermediate step between spin coating and roll-to-roll techniques. The ink is deposited onto a planar surface, and is successively dragged using a sharp blade. This technique is slower than spin coating and implies that some material will be wasted; however, small amounts of ink can be used, making this technique suitable for laboratory tests and glass modules [24].

- **Slot-die coating** is a technique that can be implemented on a roll-coater, and is compatible with roll-to-roll. It makes use of a pump to provide the ink to the meniscus, which then forms a continuous wet layer. Slot-die coating allows to produce stripes with a defined width, and a thickness that can be controlled by either varying the speed of the roll-coater drum or the flow rate of the pump. Traditional slot-die coating allows for temperature control of the substrate only, but applying heat to the coating head has been proven beneficial to the performance of both fullerene-based and fullerene-free organic solar cells [25, 26].

Printing

Printing techniques can be defined as those that allow to transfer a pattern onto a substrate, with or without contact (in the case of inkject printing, for instance).

- **Gravure printing** is often used to print magazines. A gravure cylinder goes through an ink bath, and the engraved cavities transfer the ink to the substrate by surface tension. This technique is roll-to-roll compatible, and has been used, for instance, for the fabrication of entire devices based on the blend P3HT:PCBM [27].

- **Flexographic printing** relies on a printing plate with a relief pattern. A fountain roller provides ink to an anilox roller, which is in contact with the printing roller. This technique is roll-to-roll compatible. It is often used to print conductive grids and electrodes.

- **Screen printing** can be divided in two categories: flat-bed screen printing and rotary screen printing. Flat-bed screen printing allows for very thick films (wet thicknesses between 10 and 500 micron) to be formed. A squeegee goes through a screen that has slits in the desired pattern and pushes the ink paste onto the substrate. This technique is not fully scalable. Rotary screen printing is the roll-processing analogue of flat-bed screen printing. The substrate moves on a roll-coater while a fixed squeegee pushes the ink out of a rotating mask. This technique is fully scalable and roll-to-roll compatible. It has been used to print the electrodes of OSCs [28] as well as for active layers [29].

Sputtering

Sputtering is a technique based on ion bombardment. A material is sputtered by a plasma (usually Argon), which dislodges its atoms and deposits them on the target. The resulting layers have high uniformity and good control of the thickness is possible; however, this technique is only partially scalable due to its discontinuous nature. It has been demonstrated that including sputtering in a roll-to-roll process for OSC fabrication is possible [30].

Thermal evaporation

During thermal evaporation, a voltage is applied to a boat containing the material that needs to be evaporated, melting it. At vacuum, the material

evaporates and deposits on the substrate, which is shadowed with masks. This technique allows for precise control of the thickness, but does come with some waste, and requires vacuum, making this technique only partially scalable as well.

3.2 Non-fullerene acceptors

Fullerene derivatives have been widely employed as acceptor materials for OPVs thanks to their high electron affinity and mobility [31]. Additionally, thanks to their spherical shape, these materials show optimal phase separation in the bulk heterojunction [32], which is necessary for efficient exciton dissociation at the donor/acceptor interfaces.
Materials such as $PC_{61}BM$ and $PC_{71}BM$ ([6,6]-pheny-C61/C71-butyric acid methyl ester) have been used extensively and can yield devices with PCEs higher than 11% [19] , but that value has proven hard to surpass, and fullerene derivatives seem to impose a limit on the development of polymer solar cells. On top of the difficulty to produce better performing devices, fullerene-based acceptors show drawbacks such as high costs of production and purification, fast degradation in air, a limited absorption of visible light, and hard to tune energy levels[33]. In the very recent years, developing an alternative to these materials has become a priority for polymer solar cell research, and to this day, the novel family of fullerene-free acceptors have significantly boosted the performances of OPVs.

Non-fullerene acceptors have proven to be easier to synthetize and purify, and show high stability as well as superior light absorption compared to their fullerene counterparts [24]. At lab-scale, they have allowed the achievement of 17.3% PCE in tandem solar cells [18], and over 16% PCE in single-junction devices [34].

3.3 P3HT:O-IDTBR

Poly(3-hexylthiophene-2,5-diyl (P3HT) is a semiconducting polymer, and belongs to the larger family of polythiophenes. Its side chain allows the conjugated backbones to have a π - π stacking, which is why this polymer is used in organic electronics. P3HT has been used in OPV research for a long time [35, 36, 21]. Its stability [37, 28], easy synthesis [38, 39] and compatibility

with roll-to-roll processing [24] make it a perfect candidate for the upscaling of this technology. P3HT is commonly paired with [6,6]-phenyl-C61-butyric acid methyl ester (PCBM), but a new acceptor developed by Holliday et. al. [40] has been of interest in the last couple of years.

The new acceptor IDTBR, developed specifically to match with P3HT, has the structure of the acceptor FBR [1], but the fluorene core is replaced with an indiacenodithiophene unit. When the indiacenodithiophene core is alkylated with linear n-octyl, the material takes the name O-IDTBR. IDTBR has a planar structure, which translates into a crystallization more suited for exciton dissociation, as well as a shift in absorption towards longer wavelengths compared to FBR [40]. This shift is particularly interesting because P3HT absorbs in the range of 300 nm - 600 nm, and having a donor/acceptor system with complementary absorption spectra is beneficial for the performance of the devices [41]. Absorbance spectra of both singular materials, as well as those of the blend are provided in this work.

Holliday et. al. [40] have demonstrated a 6.3 % PCE in cells with an area of 0.1 cm^2 using this system. More recently, modules of 60 cm^2 using doctor blading and slot-die coating on a glass substrate have been manufactured using P3HT:O-IDTBR [24], reaching efficiencies of around 5%.

3.4 Towards commercialization

In order to achieve the goal of commercialization of this technology the 10-10 targets [22] must be met: efficiencies of 10% and 10 years of stability.
It must be underlined that these targets should be met by devices fabricated under fully scalable conditions in order to reach commercialization, because the performance of these devices changes drastically when upscaling. To enter the market, research should focus on finding systems that are suited to roll-to-roll techniques, and then work on optimizing of the efficiency.

[1] FBR stands for (5Z,50Z)-5, 50-(9,9-dioctyl-9H-fluorene-2,7-diyl)bis [2,1,3-benzothiadiazole-7, 4-diyl(Z)methylylidene]bis(3-ethyl-2-thioxo-1,3-thiazolidin-4-one)

3.5 Purpose of this work

To this day, there are no records of ITO-free, flexible, P3HT:O-IDTBR-based devices fabricated with only roll-to-roll compatible techniques in large areas (1 cm^2). The present work provides an optimization process that can be applied to roll-processing techniques such as slot-die coating and flexographic printing, in an effort to produce large-area solar cells (singular, 1 cm^2 cells as well as larger modules) and improving their efficiency as the procedure moves forward.
Reports have shown that the morphology of the active layer can be improved with by optimizing the temperature of the roll-coater drum as well as that of the slot-die head [25, 26]. This study aimed at optimizing the active layer using temperature-controlled slot-die coating, varying both the roll coater's head and drum temperatures, as well as testing different thicknesses to obtain the most efficient device possible.
Subsequently, the HTL was tested with different thicknesses by diluting the PEDOT:PSS in isopropanol (IPA), to understand whether it could be possible to reduce material consumption and obtain semitransparent layers without sacrificing performance.
Finally, four different electrode materials were tested: flexographically printed silver, and thermally evaporated silver, copper and gold. The motivations behind this study were to test if including a vacuum step in the fabrication process could yield significant improvements, as well as whether it would be worth it to include an expensive material such as gold, and, finally, to check if a cheaper metal like copper could still yield performing devices.

An inverted configuration was used, due to the flexible substrate (flextrode) that was available to us. This included the PET substrate, a flexographically printed silver grid as transparent electrode, a layer of PEDOT:PSS and a layer of ZnO nanoparticles as ETL (both slot-die coated) [42].
The different layers of our devices are shown in Figure 3.1.

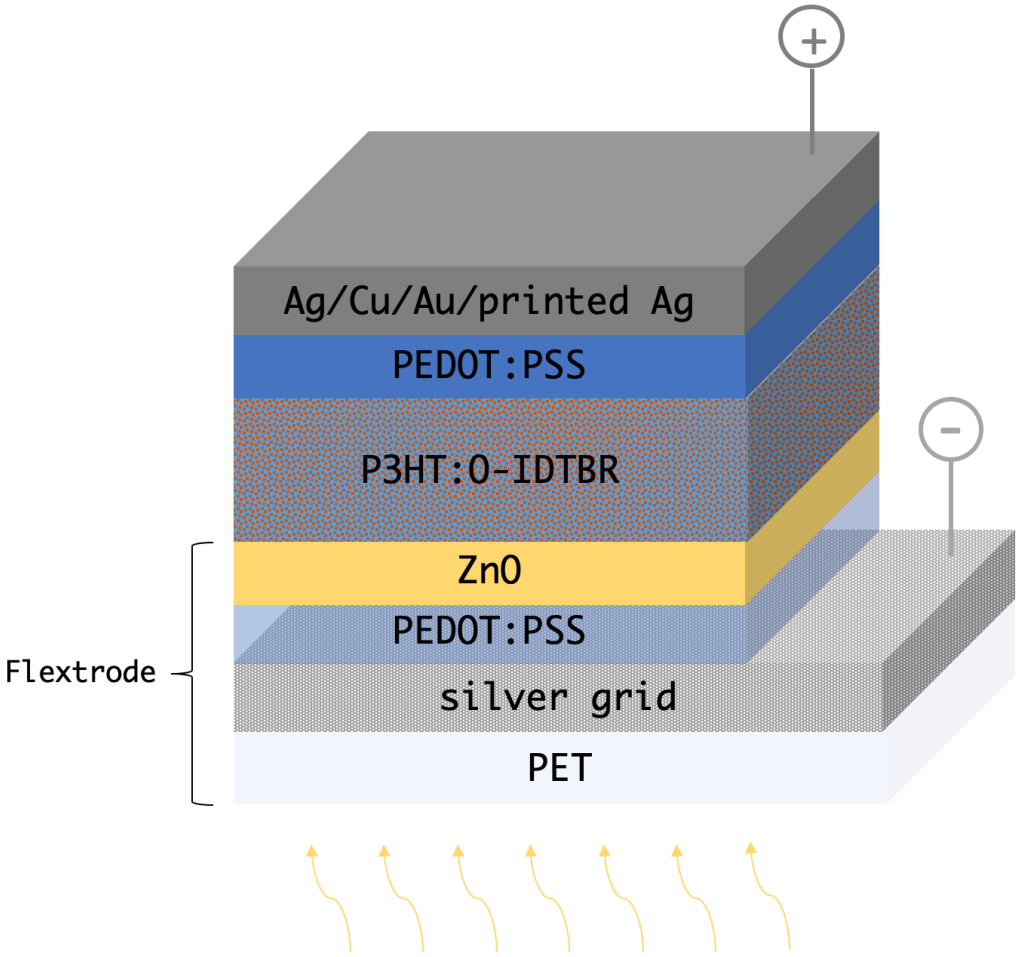

Figure 3.1. Inverted OPV structure used for this project

Chapter 4

Materials and methods

The entirety of this project was carried out in the laboratories of DTU Energy, Risø Campus, Roskilde.

4.1 Materials

4.1.1 Active layer

Donor: P3HT

The donor material, P3HT, was purchased from Ossila Materials, batch number 1011. This specific batch ensured 97.6% regioregularity and around 60 kDa molecular weight, both proven to influence the performance of OSCs [39].

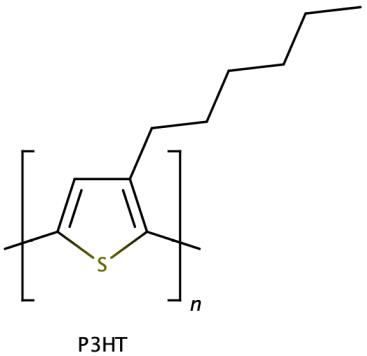

Figure 4.1. Chemical structure of P3HT

Acceptor: O-IDTBR

The small molecule O-IDTBR was purchased from 1-Materials Inc. Its chemical structure is shown in Figure 4.2.

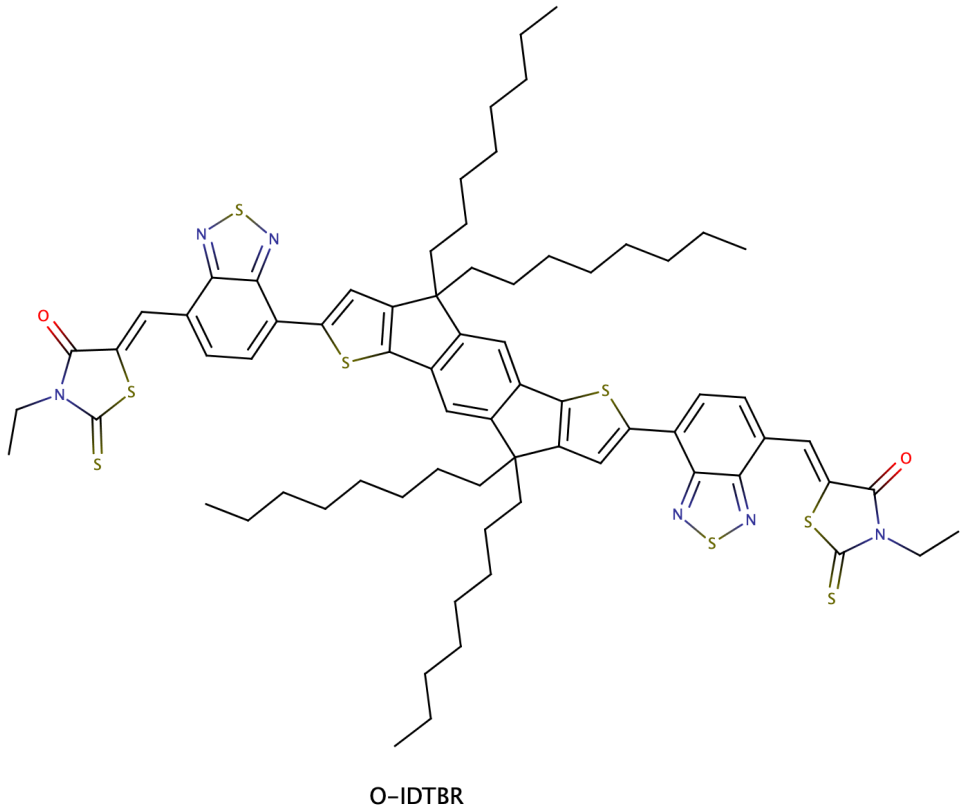

Figure 4.2. Chemical structure of O-IDTBR

4.1.2 Hole transport layer: PEDOT:PSS

PEDOT:PSS, or poly(3,4-ethylenedioxythiophene) polystyrene sulfonate, is a conductive polymer known for its tunable electrical conductivity, transparency in the visible range, environmental stability and flexibility [43]. It is composed of PEDOT, a conjugated polymer carrying positive charges, and PSS, a sulfonated polystyrene that is partially deprotonated, and carries negative charges.
For the purpose of this study, it was purchased from Haereus CLEVIOS FET.

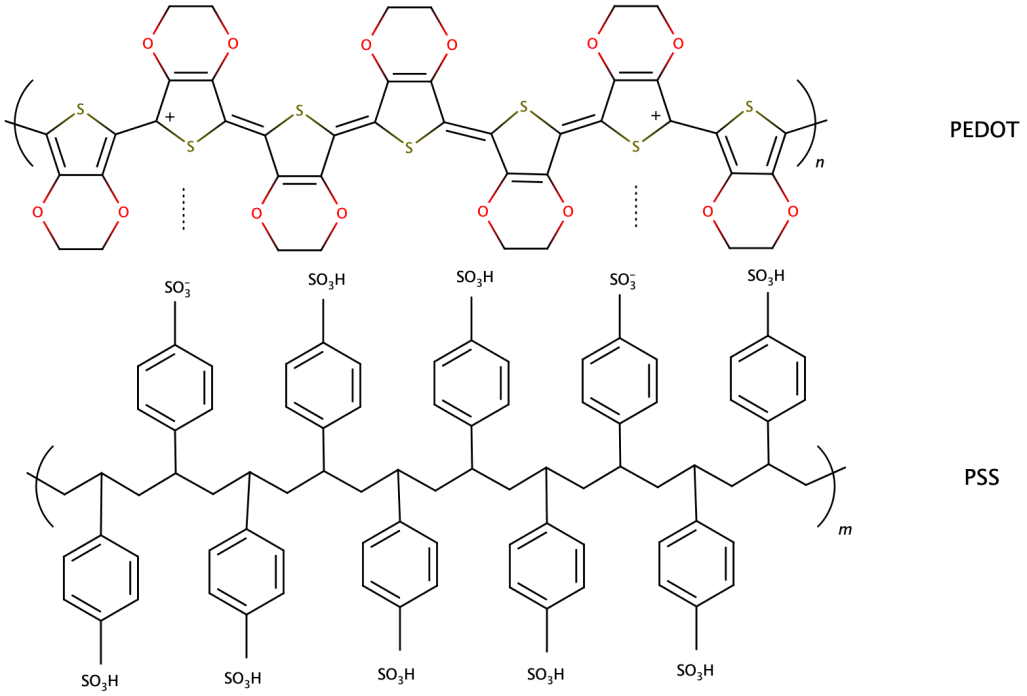

Figure 4.3. Chemical structure of PEDOT:PSS

4.1.3 Electrodes

Silver paste

The heat curing silver paste was purchased from DuPont (5025). It is commonly used as a paint to print electrical contacts.

Ag, Au and Cu

The silver (99.99%), gold (99.99%) and copper (99.9%) beads were purchased from Sigma-Aldrich.

4.1.4 Flextrode

The flextrode, short for flexible electrode as mentioned in section 2.1.3, was manufactured at DTU [22] (Figure 4.4). It consists of:

- a PET substrate
- a flexographically printed silver grid as the top electrode

- a slot-die coated layer of PEDOT:PSS
- a slot-die coated layer of ZnO nanoparticles to act as the ETL (ref paper)

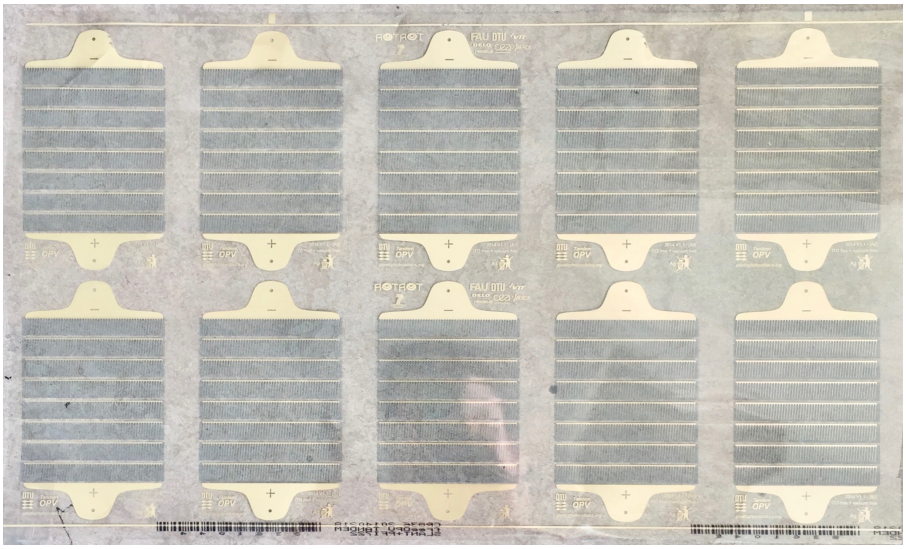

Figure 4.4. Flextrode used

4.1.5 Additional chemicals

On top of the above mentioned materials, a few solvents were used to prepare the solutions and/or for surface treatment purposes (Appendix A for details on these steps).
The isopropanol, butanol and dichlorobenzene were purchased from Sigma Aldrich Inc.

4.2 Methods

4.2.1 Fabrication

Mini roll-coater

The majority of the fabrication procedure (excluding the evaporated electrodes) was done using a roll-coater (Figure 4.5). This piece of equipment consists of a rotating drum whose temperature and speed can be controlled. With this machine, the slot-die coating of the active layer and HTL, as well

as the flexographic printing of the silver electrodes were made possible thanks to the switchable heads.

Figure 4.5. Mini roll-coater with slot-die head inserted

Hot slot-die coating

As previously mentioned, this variation on slot-die coating has proven successful in the optimization of active layer deposition for OSCs. In our setup, the slot-die head was simply heated using a resistor and controlled with a thermocouple. The temperature of the head is independent from the temperature of the drum.

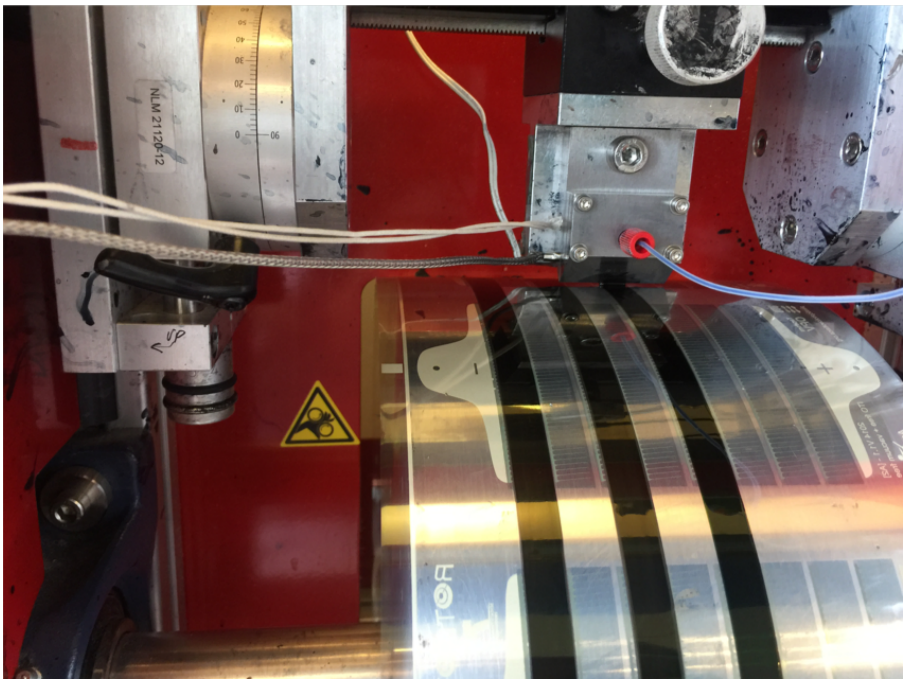

Figure 4.6. Temperature-controlled slot-die head in the process of coating

Flexographic printing

Electrode printing was performed using a manual flexographic printing roller (Figure 4.7) attached to the mini roll-coater. The silver paste was then applied onto the printing head with a sponge roller, then pressed onto the rotating substrate.

The chosen flexographic head printed a finger-like pattern onto the HTL with a total area of $1cm^2$.

Figure 4.7. Flexographic printing rolls

Thermal evaporation

The evaporated Ag, Au and Cu electrodes were deposited using a shadow mask in a thermal evaporator, to produce an active area of $1cm^2$. Figure 4.8 shows an example of shadow masks on the rotating plate of the evaporator.

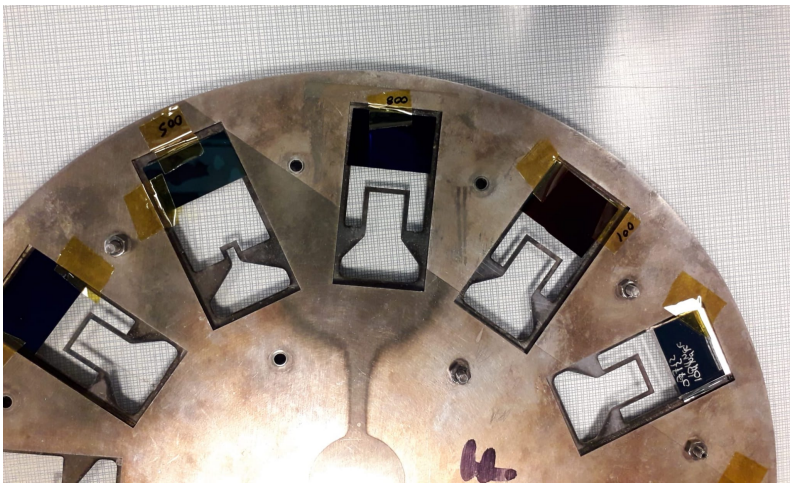

Figure 4.8. Example of shadow masks

4.2.2 Characterization

Before being characterized, the solar cells were activated with a short reverse bias current (around 600 mA). This step is necessary to obtain the correct I-V response.

For this study, the J-V curves were extracted using an in-house Sun Simulator with a Xenon lamp source and the "Solar Cell Test" software from Infinity PV. The calibration was done using a monocrystalline silicon reference cell certified by Fraunhofer, under AM 1.5G, using 1000 W/m^2.

The EQEs, absorbance and transmittance spectra were obtained using the QEX10 measuring system from PV Measurements Inc.

The active layer morphology images were obtained using a Danish Micro Engineering AFM DS95-50 (Figure 4.9).

Figure 4.9. Atomic Force Microscope Used

Chapter 5

Results and discussion

As previously mentioned, the active layer is the area of the solar cell where excitons are created, and where they dissociate. Therefore, the morphology of this layer has a key role in the performance of the cell [44, 45, 46] . Practically, it can be modified through an optimization process of the active layer, which includes changing the drying kinetics of the blend through temperature [26], as well changing the thickness of the coating.
The following sections provide an optimization procedure that concerns the active layer made of P3HT:O-IDTBR, the HTL made of PEDOT:PSS, and the four electrodes, namely printed and evaporated silver, evaporated copper, and evaporated gold. The purpose of this procedure was to understand how parameters such as drying temperature, thickness and transparency could affect the behaviour of the final devices, in an effort to optimize them in a completely scalable way.

5.1 Active layer optimization

The active layer optimization has been carried in the following way: the temperature was varied in the drum of the roll-coater (DT), until one that would yield a significant improvement in PCE was found. This temperature was then set as the optimal DT for the next experiment. Subsequently, the head temperature (HT) was also varied and, once again, fixed to the value that improved the efficiency the most. Finally, the thickness of the active layer was varied by simply modifying the speed and flow rate of the machine, whilst keeping the optimal temperature combination in the bed and head of the roll-coater. All experimental steps taken during this study have

been described in detail in appendix A. The following sections aim at briefly explaining the parameters variations made, showing the results in terms of photovoltaic and optoelectrical performance and discussing their impact on the final devices.

5.1.1 DT optimization

The temperature of the roll-coater bed is of prime importance when it comes to the morphology of the active layer. This is because it strongly influences the drying kinetics of the film, therefore modifying its structure once set [26, 25]. Specifically, it has been proven that in slot-die coating, increasing temperatures in both the bed and the head of the roll-coater reduces the size of the grains in the crystalline structure of the material for non-fullerene acceptor OSCs [46]. AFM images obtained during the active layer optimization are provided in section 5.1.4, aiming at shedding more light on this topic.

Experimental setup

The aim of this test was to observe how the increase of temperature of the drum of the roll-coater, changed from RT to 90°C, would impact the efficiency of the final device. This was done whilst keeping HT equal to RT, a fixed drum speed throughout the whole experiment and using an undiluted PEDOT:PSS mixture as HTL, as well as flexographically printed Silver electrodes. The stripes were simply coated on the substrate modules three by three, with BT: RT, 50°C, 60°C, 70°C, 80°C and 90°C. We made sure that the stripes were dry before increasing the dt and starting with the next ones.

Characterization and results

Fig 5.1 shows the average PCE based on two encapsulated devices as a function of BT. It is possible to see a substantial difference in efficiency between the RT cells and the rest. This is not surprising as RT on the drum does not allow for uniform drying of the layer, and the rotating movement of the drum might actually create islands of material while it is still wet. The opposite must be noticed too: the stripes obtained at 80°C and 90°C DT also show lower efficiencies compared to the 60°C and 70°C ones. This could mean that above a certain threshold, a high temperature might start annealing the organic film under oxygen exposure, which can damage the layer; alternatively, this could simply mean that this temperature yields a suboptimal morphological structure of the blend. Evidently, the best performance is obtained

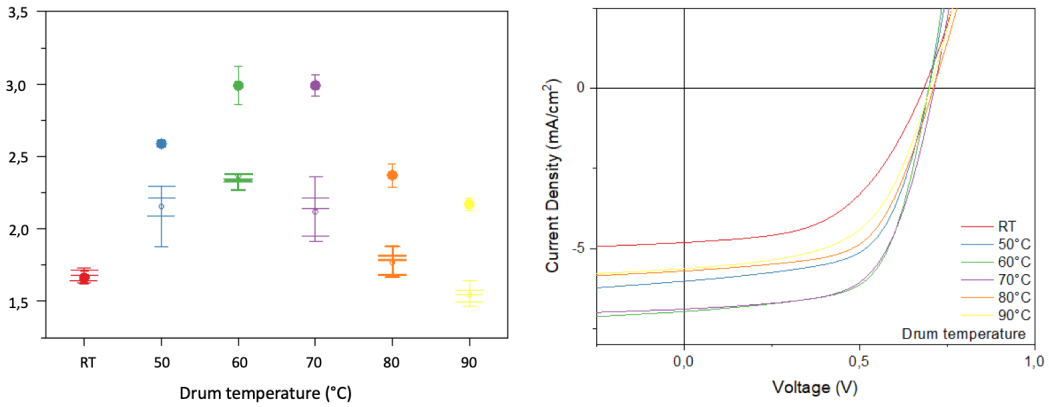

Figure 5.1. Average PCEs of non-encapsulated devices (I-shaped boxes) and encapsulated devices (dots) (left), JV curves (right)

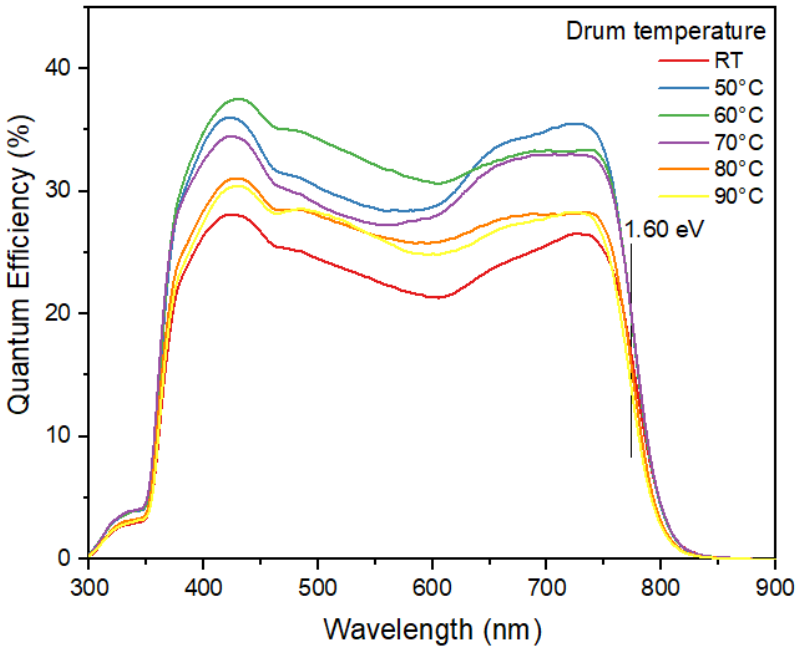

Figure 5.2. EQE for drum temperature test

with a 60°C or 70°C temperature in the drum. For the sake of optimizing the energy consumption of this whole process, 60°C was chosen as the optimal

temperature in this test.

5.1.2 HT optimization

Experimental setup

The DT was fixed to 60°C, as well as all the other layers as previously mentioned (surface treatment using butanol, HTL and electrodes). The temperatures used in this test were 40°C, 60°C, and 80°C. This was done to monitor the behavior of the PCE at the optimal BT, as well as for slightly lower and higher temperatures respectively. It is important to mention that higher temperatures were also tested, but the heat created bubbles of active material inside the coater head, leading to an uneven coverage of the film and were therefore discarded.

Characterization and results

The results from this test can be summarized in fig 5.3. The data representing HT=RT comes from the previous experiment, in the case where BT=60°C (HT=RT due to the nature of the experiment). Figure 5.3 shows that the most efficient temperature is once again 60°C: matching drum and head seems to yield optimal results. This is in agreement with our expectations [26, 25]. It is particularly interesting to notice, from table 5.1, that the average Jsc is much higher in this case, which directly translates into a higher charge extraction inside the device.

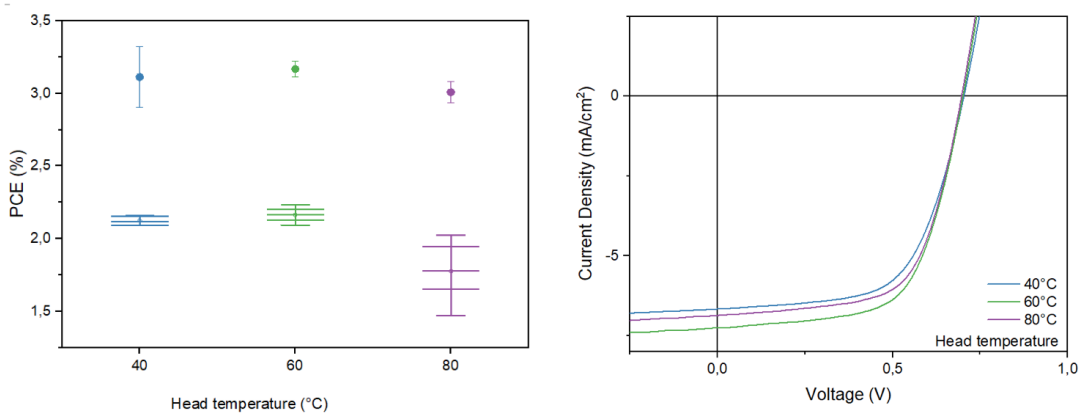

Figure 5.3. Average PCEs for non-encapsulated (I-shaped boxes) and encapsulated devices (dots) (left), JV curves of encapsulated devices (right)

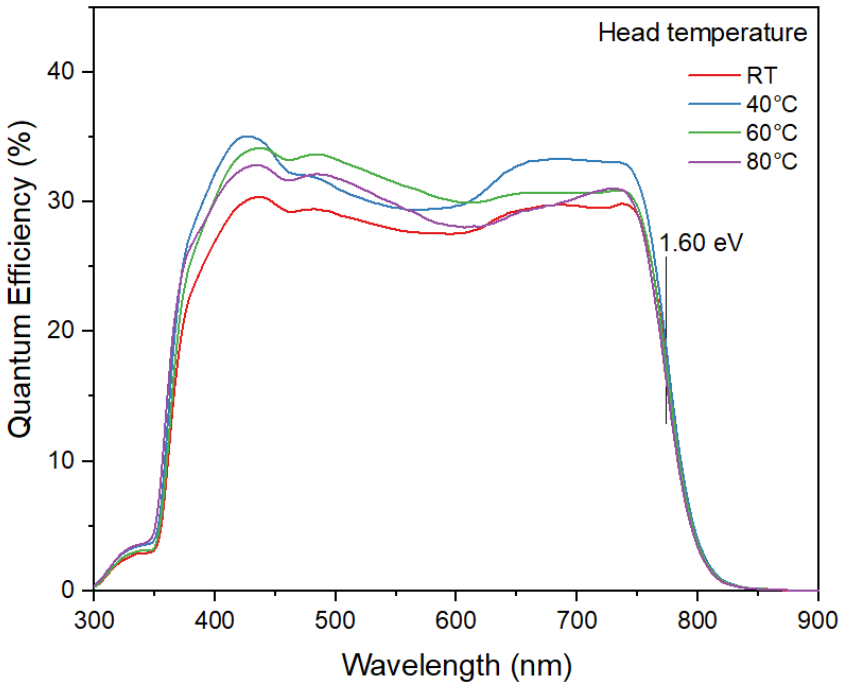

Figure 5.4. EQE for head temperature test

HT (°C)	**DT (°C)**	**PCE (%)**	**FF (%)**	**Jsc (mA/cm^2)**	**Voc (V)**
RT	RT	1.71 (1.66±0.04)	51.88 (51.75±0.13)	4.81 (4.72±0.09)	0.68 (0.68±0.01)
RT	50	2.59 (2.59±0.01)	61.80 (60.68±1.12)	6.02 (6.07±0.05)	0.70 (0.70±0.01)
RT	60	3.12 (2.99±0.13)	64.30 (64.63±0.33)	6.97 (6.64±0.32)	0.70 (0.70±0.01)
RT	70	3.07 (2.99±0.08)	62.39 (63.00±0.61)	6.89 (6.69±0.20)	0.71 (0.71±0.01)
RT	80	2.45 (2.37±0.08)	60.38 (59.77±0.61)	5.71 (5.64±0.07)	0.71 (0.70±0.01)
RT	90	2.21 (2.17±0.04)	56.05 (52.70±3.35)	5.63 (5.85±0.22)	0.70 (0.71±0.01)
40	60	3.32 (3.11±0.21)	63.58 (62.77±0.81)	7.47 (7.07±0.40)	0.70 (0.70±0.01)
60	60	3.22 (3.17±0.06)	63.41 (63.50±0.08)	7.26 (7.15±0.11)	0.70 (0.70±0.01)
80	60	3.08 (3.01±0.07)	64.35 (64.44±0.10)	6.87 (6.70±0.17)	0.70 (0.70±0.01)

Table 5.1. Maximum and average (inside parentheses) photovoltaic parameters for both HT and DT experiments

5.1.3 Thickness optimization

As a last step, different dry thicknesses for the active layer were tested with the optimal temperature to see if it would be possible to reduce material consumption while still yielding the same – or better – performances.

Experimental setup

The thickness was varied by controlling the flow rate of the head with a constant drum speed, as shown in formula [ref. formula nella parte di metodi]. Specifically, knowing that the dry thickness of P3HT:O-IDTBR obtained in the past experiments was equal to 480 nm, we decided to test both thinner and thicker layers, of 360 nm, 600 nm and 720 nm respectively. The exact experimental procedure is fully described in appendix A.

Characterization and results

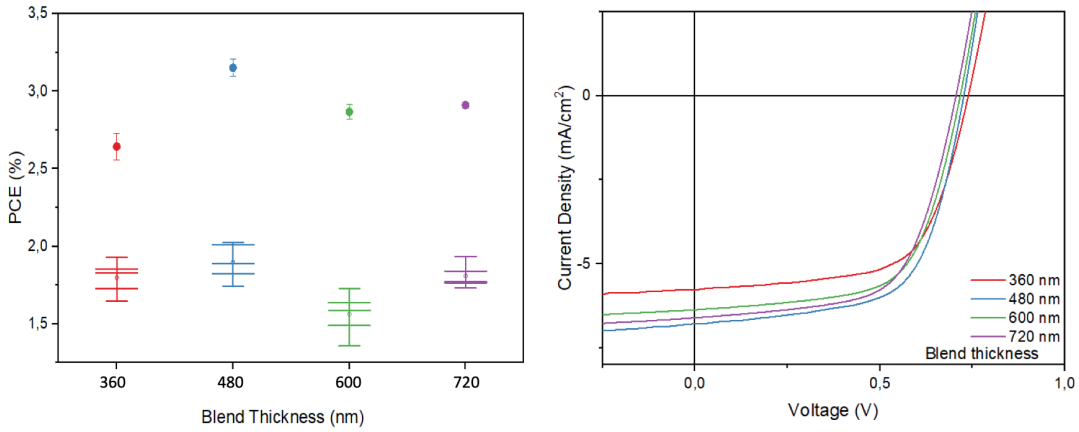

Figure 5.5. Average PCEs of non-encapsulated devices (I-shaped boxes) and encapsulated devices (dots) (left), J-V curves (right)

Fig. 5.5 shows the average PCEs as a function of the thickness. It is possible to see that the highest efficiencies were obtained with the 480 nm layers, and this is confirmed by the EQE curves. It is important to optimize the thickness of the active layer: if the film is too thin, light might go through it without

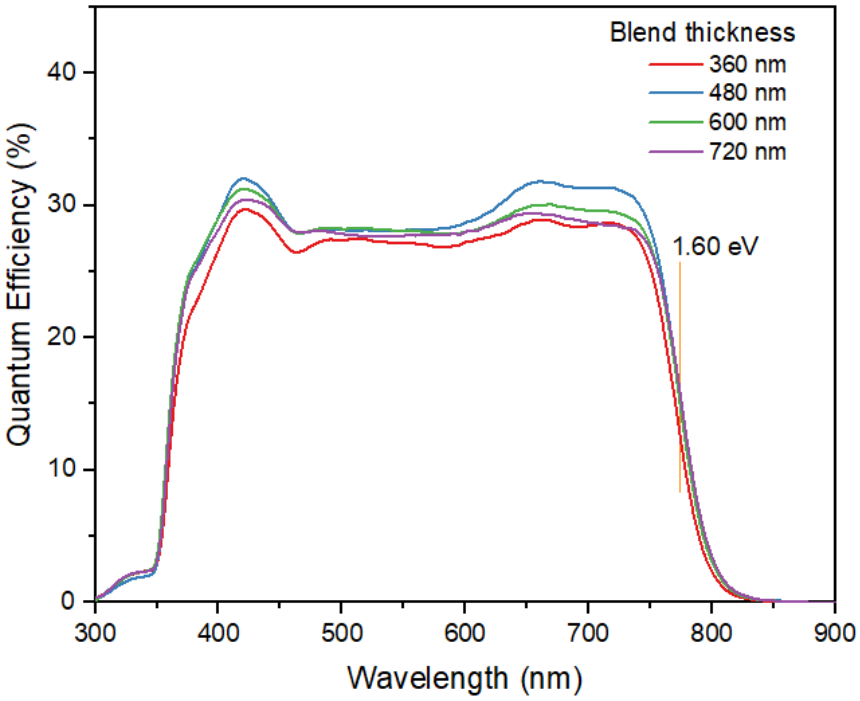

Figure 5.6. EQE for thickness test

a chance to be absorbed, whereas if the layer is too thick, recombination is more likely to happen [47].

Flow rate (mL/min)	**Thickness (nm)**	**PCE (%)**	**FF (%)**	**Jsc (mA/cm^2)**	**Voc (V)**
0.06	360	2.73 (2.64±0.09)	64.19 (64.01±0.18)	5.75 (5.59±0.16)	0.74 (0.74±0.01)
0.08	480	3.22 (3.15±0.06)	63.41 (63.12±0.61)	7.26 (6.96±0.21)	0.70 (0.72±0.01)
1	600	2.91 (2.87±0.05)	63.91 (63.98±0.07)	6.36 (6.23±0.13)	0.72 (0.72±0.01)
1.12	720	2.93 (2.91±0.02)	63.01 (61.891.12)	6.60 (6.67±0.07)	0.71 (0.71±0.01)

Table 5.2. Maximum and average PV parameters for the thickness test

5.1.4 Surface morphology after optimization

With this optimal configuration in mind, a comparison of the surface morphology under different circumstances was done using Atomic Force Microscopy. Specifically, fresh layers of P3HT:O-IDTBR with a thickness of 480 nm were coated for the sole purpose of this characterization at temperatures (DT/HT) RT/RT, 60/RT, 60/60. This was done to understand the impact of each temperature variation on the crystallinity of the layer. As Figure 5.7 shows, the RT/RT layer shows larger grains compared to the rest, and as a general trend, grains tend to become smaller as our process becomes optimal. In fact, the RT/RT layer has an RMS roughness of 77 nm, followed by the 60/RT layer with 28 nm and finally the 60/60 layer with 25 nm.
In light of our results, we can see that the layers with the lowest roughness were also those who yielded the highest average PCEs and J_{SC}. We can conclude that, as expected, smaller grains lead to an easier charge dissociation.

5.1.5 Absorbance spectra after optimization

As a final result for this test, the absorbance spectra of blend before and after optimization, as well as those of the donor and acceptor separately, are presented:
It can be seen that the inflexion points (the points where the absorbance drops drastically, indicating that radiation beyond that value cannot be harvested) do not change with the temperature of the blend. Rather, the absorbance is increased (yellow area) in the 60/60 blend, which explains the gain in J_{SC} when going from RT/RT to 60/60 conditions, since an increase in absorbance is directly related to an increase of exciton generation.
Charge extraction is mostly attributed to the HTL and the electrodes, which will be discussed in the following sections.

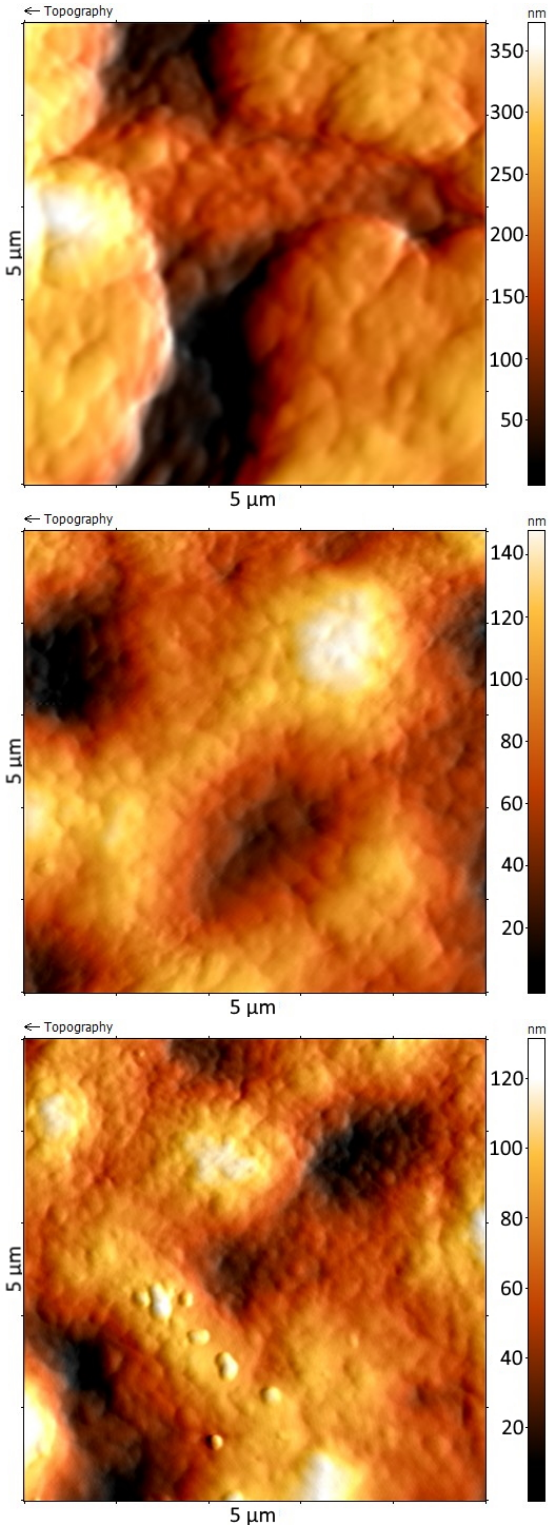

Figure 5.7. AFM images for RT/RT (top), RT/60 (middle) and 60/60 (bottom)

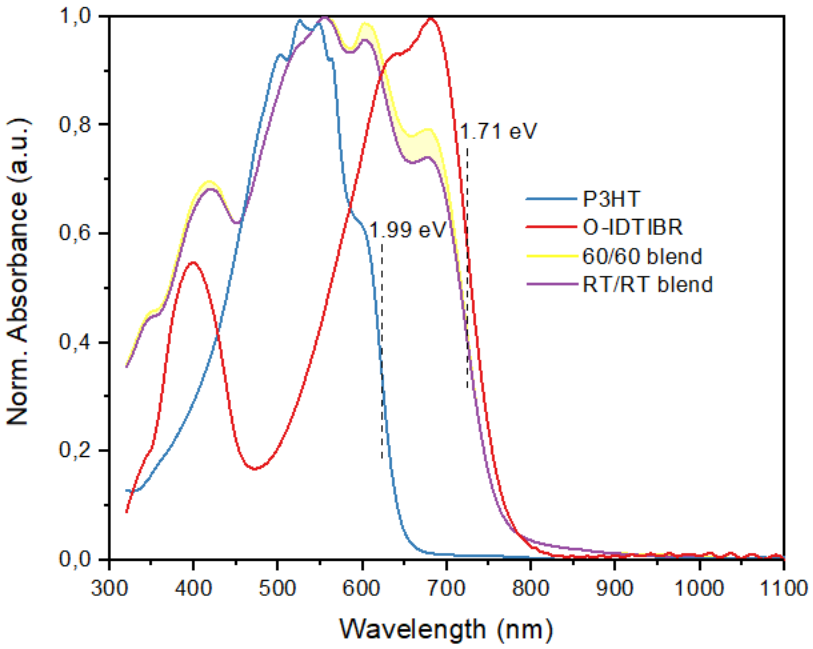

Figure 5.8. Absorbance spectra of the donor and acceptor materials, as well as the blend at RT/RT and 60/60 conditions

5.2 Hole transport layer optimization

Since part of this study was also dedicated to optimizing material usage and the energy necessary for the fabrication process, it was important to try and reduce the quantity of PEDOT:PSS used as much as possible, whilst still obtaining high performing devices. This is the purpose of this section.

Experimental setup

For this experiment, pure PEDOT:PSS was diluted in IPA in three different solutions, with ratios IPA:PEDOT 1:1, 2:1, and 3:1. The purpose of reducing the amount of PEDOT:PSS concentration and adding a solvent such as IPA to the solution is to create a film that is not only increasingly transparent as the amount of IPA increases, but also that dries at a fraction of the time. This also allows to reduce costs, since IPA has a cost negligible to that of PEDOT:PSS. Furthermore, using IPA directly in the HTL solution was done to try and avoid the surface treatment step (butanol) between active layer and PEDOT:PSS, to increase adhesion between the two layers. It must be kept in mind that the temperature optimization was set from the previous experiment and that the HTL was always dried at 70°C, so there was no variable temperature in this experiment.

The layers were coated with different parameters, since using the same ones as pure PEDOT would not yield uniform coatings. Specifically, the speed was kept constant but the flow rates were decreased proportionally to the ratio of dilution.
This system yielded satisfactory layers in terms of width, i.e. there were no problems with the thinner solutions running down the substrate, etc. However, not all layers of HTL adhered to the active layer, specifically the 1:1. In this case, the butanol surface treatment was performed. Additionally, the 1:1 and 2:1 solutions created non-uniform layers in term of coverage: the IPA and PEDOT:PSS did not mix enough and the resulting coatings showed islands of PEDOT:PSS separated from more transparent areas.

As the device fabrication went on, it was clear that the solutions could not handle the flexographically printed silver electrodes as well, hypothetically due to their much lower thicknesses. This resulted in a lot of the cells not working, and the remaining ones behaved poorly. The solution to this problem was to thermally evaporate silver instead of printing it.

Characterization and results

The results discussed in this section come from devices obtained with pure PEDOT:PSS, 1:1, 2:1 and 3:1 solutions, on top of the optimized active layer. Figure 5.9 shows the JV curves for both evaporated and printed silver electrodes for each solution, and table 5.3 shows the maximum and average PV parameters obtained.

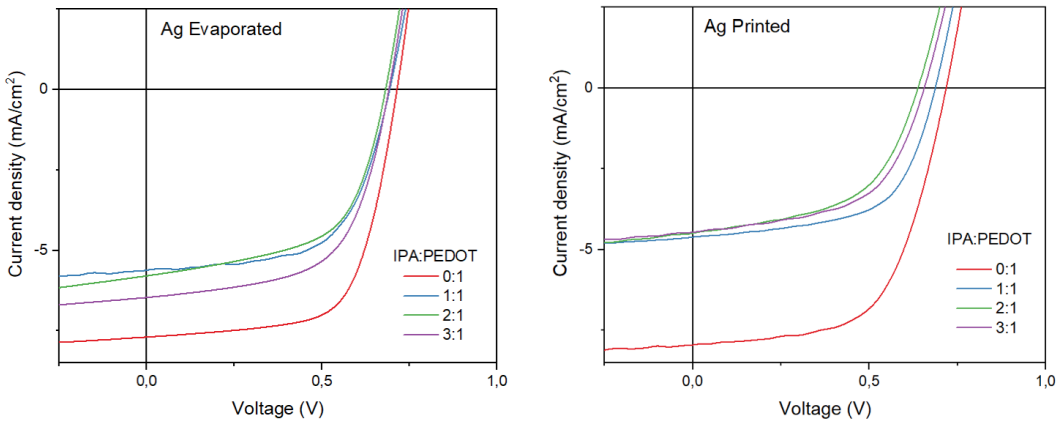

Figure 5.9. JV curves for HTL experiment, with evaporated (left) and printed (right) silver electrodes

PEDOT/Ag Print	**PCE (%)**	**FF (%)**	**Jsc (mA/cm2)**	**Voc (V)**	Eg^{PV} **(eV)**
0:1	3.45 (3.30±0.10)	60.48 (60.42±0.19)	7.94 (7.68±0.18)	0.72 (0.71±0.01)	1.60
1:1	1.90 (1.82±0.07)	60.98 (59.89±1.09)	4.61 (4.51±0.10)	0.68 (0.68±0.01)	1.61
2:1	1.53 (1.53±0.01)	53.52 (52.91±0.61)	4.49 (4.51±0.04)	0.66 (0.65±0.01)	1.62
3:1	1.63 (1.53±0.10)	55.81 (55.35±0.46)	4.46 (4.30±0.16)	0.66 (0.64±0.01)	1.65
PEDOT/Ag Evap					
0:1	3.64 (3.35±0.22)	65.28 (64.21±0.81)	7.69 (7.01±0.53)	0.73 (0.72±0.01)	1.60
1:1	2.40 (2.40±0.10)	61.68 (61.68±1.09)	5.61 (5.61±0.10)	0.69 (0.69±0.01)	1.60
2:1	2.30 (2.21±0.10)	58.35 (56.18±2.16)	5.79 (5.79±0.10)	0.68 (0.68±0.01)	1.65
3:1	2.69 (2.66±0.30)	63.25 (61.75±1.50)	6.46 (6.20±0.26)	0.70 (0.69±0.01)	1.65

Table 5.3. Maximum and average PV parameters for the HTL experiment

Unfortunately, none of the thinner HTL solutions produced improved devices, or at least not comparable to the pure PEDOT:PSS devices. This is confirmed by the EQE spectra for both types of electrodes (Figure 5.10), which show the dramatic difference between the pure and indiluted PEDOT:PSS solutions.

Photoactive role of PEDOT:PSS

The HTL optimization study has highlighted an unexpected contribution of PEDOT:PSS to the photoactivity of the solar cells. Figure 5.10 represents the EQE curves for the devices made during the HTL study. Compared with the absorption spectrum of the P3HT:O-IDTBR blend shown in the previous section (Figure 5.8), it is possible to see that the solar cell as a whole generates carriers at energies below those that the blend alone absorbs. The green dotted lines in Figure 5.10 represent the transmittance of the optimized active layer. It is interesting to see that the different thicknesses of PEDOT:PSS contribute differently to the EQE spectrum, and all of them have an inflexion point at longer wavelengths than the active layer blend. Specifically, the pure PEDOT:PSS layer (0:1 solution) absorbs radiation with energies between 1.60 eV and 1.71 eV, and transforms into photocurrent.

Table 5.3 includes the values of the photovoltaic bandgap, a value which describes the minimum energy that can be absorbed by the device as a whole [48]. This value increases with the amount of isopropanol in the solution, as can be seen from Table 5.3 and 5.10. This suggests that spectral matching of the blend with the appropriate hole transport layer makes it possible to harvest radiation with energies below the blend's bandgap.

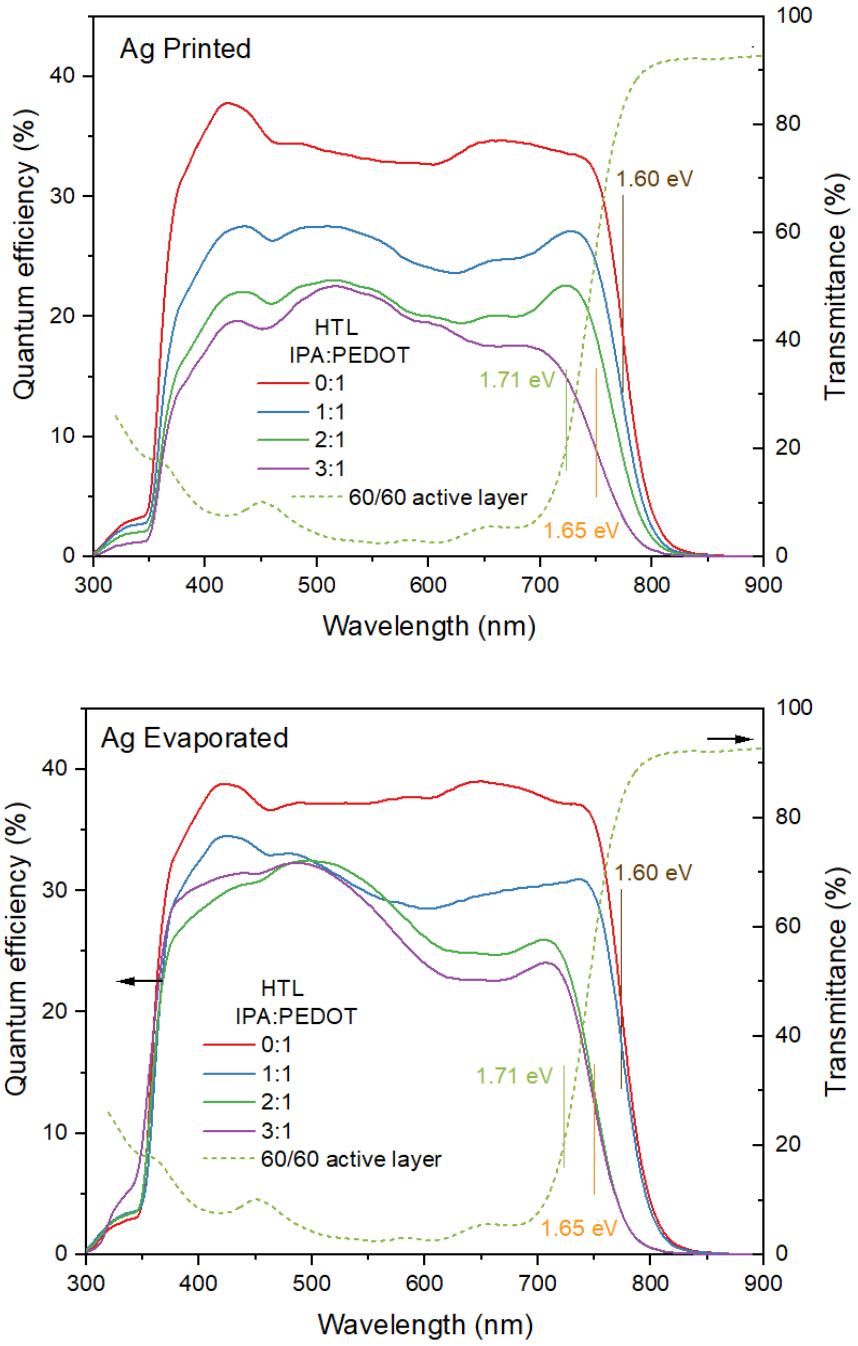

Figure 5.10. EQE curves for printed silver and evaporated silver devices within the HTL test; transmittance curve of the optimized active layer on the right-side axis

5.3 Back electrode optimization

As the final step for our study, two additional metals were added to the list of possible electrodes: copper and gold. The former was chosen due to its low cost, while the latter was chosen for its workfunction compatibility with PEDOT:PSS (Figure 5.13). The purpose of this test was to understand whether considerable savings could be made without sacrificing performance (copper) and simultaneously if a more expensive metal like gold could improve the devices enough to justify its cost. A good electrode should have low resistivity, be surface passivating and be carrier selective. For this reason, the sheet resistances of each material were measured using a 4-point probe.

Experimental setup

Thermal evaporations of 250 nm thick layers were performed for copper and gold. The details of this procedure are summarized in appendix A. The sheet resistance measurements were performed using a 4-point probe on.

Characterization and results

As mentioned above, one requirement for an efficient electrode is a low sheet resistance, and we measured this parameter for each metal deposited on a PET substrate.
The results of this measurement are summarized in table 5.4. These values might differ from the values measured on the final devices. In terms of resistivity, one would be tempted to believe that the printed silver electrodes would yield worse devices compared to the rest. However, as proven in the previous sections, printed silver electrodes produce devices comparable to those made with evaporated silver electrode. Let's now investigate the behaviour of copper and gold.

Material	**Sheet resistance** (Ω/sq)
Ag (printed)	2.26 ± 0.08
Ag (evap.)	0.277 ± 0.007
Copper (evap.)	0.587 ± 0.007
Gold (evap.)	0.589 ± 0.007

Table 5.4. Sheet resistance values for each electrode material deposited on PET

Before speaking of solar characterization, it is important to mention two points:

- the devices with copper electrodes tolerated the activating step well, with no damage. It was, however, difficult to obtain a photoresponse from the cells.

- the devices with gold electrodes were difficult to activate too, this time due to their low tolerance to the current: presumably, the cells burned instead of getting activated. This could be due to a suboptimal contact between the gold layer and the HTL, meaning that the current might be staying in the electrode instead of passing through the solar cell.

The gold electrodes were the least performing ones, as shown in Figure 5.11. The cells showed a maximum PCE of 2.06%, with the lowest FF of all four electrodes (57.48%) and J_{sc} (4.95% compared to, for instance, 8.07% for evaporated silver devices). The particularly low value J_{sc} suggests that gold has a low hole selectivity; its workfunction is more suited for electron collection.

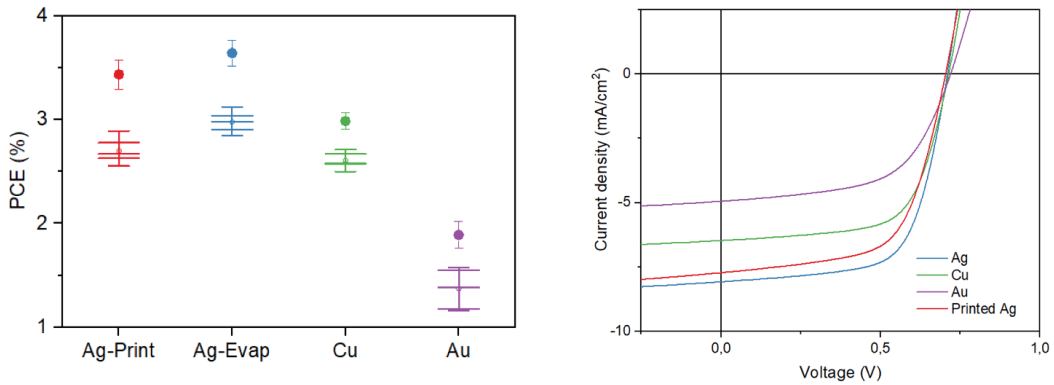

Figure 5.11. Average PCEs for non-encapsulated (I-shaped boxes) and encapsulated devices (dots) (left), J-V curves (right)

Similarly, the copper devices that were successfully switched did not show results comparable to the printed or evaporated silver devices. Whilst the FF was sufficiently high (with a maximum of 64.73%), the PCE and Jsc simply did not reach high enough values to be considered an alternative.

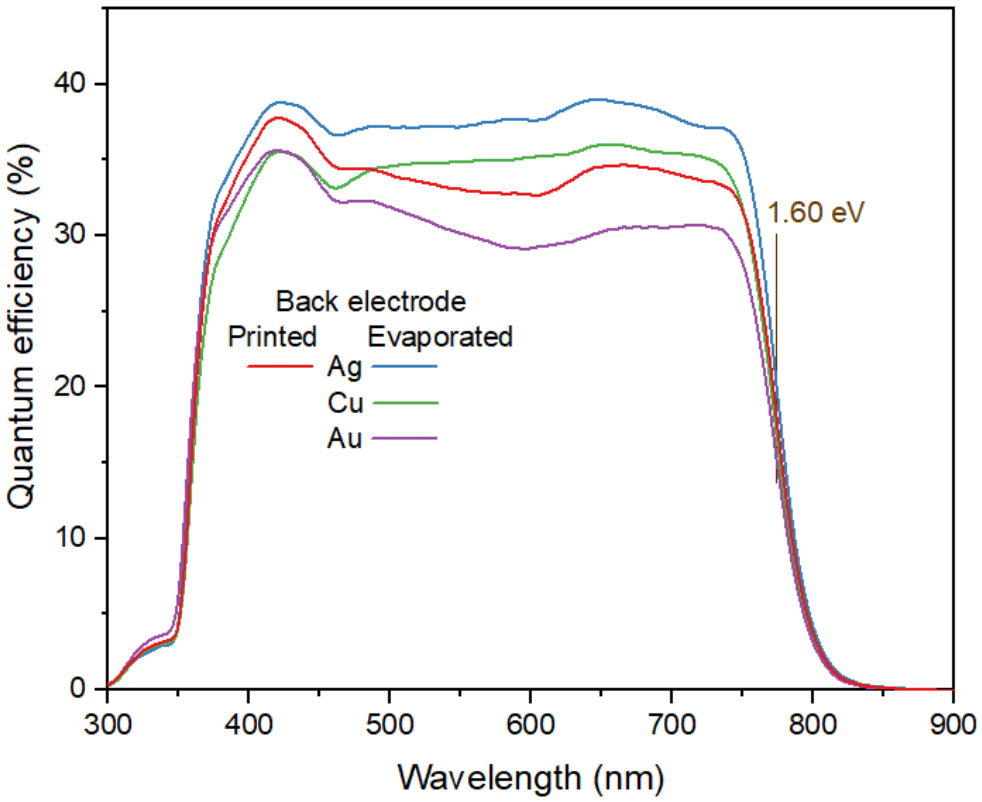

Figure 5.12. EQE curves of devices with different electrode materials

Material	**PCE (%)**	**FF (%)**	**Jsc (mA/cm^2)**	**Voc (V)**
Ag-Print	3.44±0.14	63.30±0.82	7.64±0.24	0.71±0.01
Ag Evap	3.64±0.12	66.01±0.73	7.74±0.28	0.71±0.01
Cu Evap	2.98±0.08	64.27±0.66	6.41±0.17	0.73±0.01
Au Evap	1.89±0.13	56.78±1.15	4.61±0.32	0.72±0.01

Table 5.5. Average PV parameters for different electrode materials

Table 5.6 highlights the record efficiencies obtained for this system: printed silver reached 3.59%, while evaporated silver reached 3.8%. These values correspond to the champion devices for this study.
Figure 5.13 shows that silver has a work function that allows for hole selectivity more than the other metals. This could be the reason for silver being

Material	PCE (%)	FF (%)	Jsc (mA/cm^2)	Voc (V)
Ag-Print	**3.59**	64.27	7.9	0.71
Ag Evap	**3.8**	67.27	8.07	0.7
Cu Evap	3.04	64.73	6.47	0.73
Au Evap	2.06	57.48	4.95	0.73

Table 5.6. Maximum PV parameters for different electrode materials

the best performing electrode in this study.

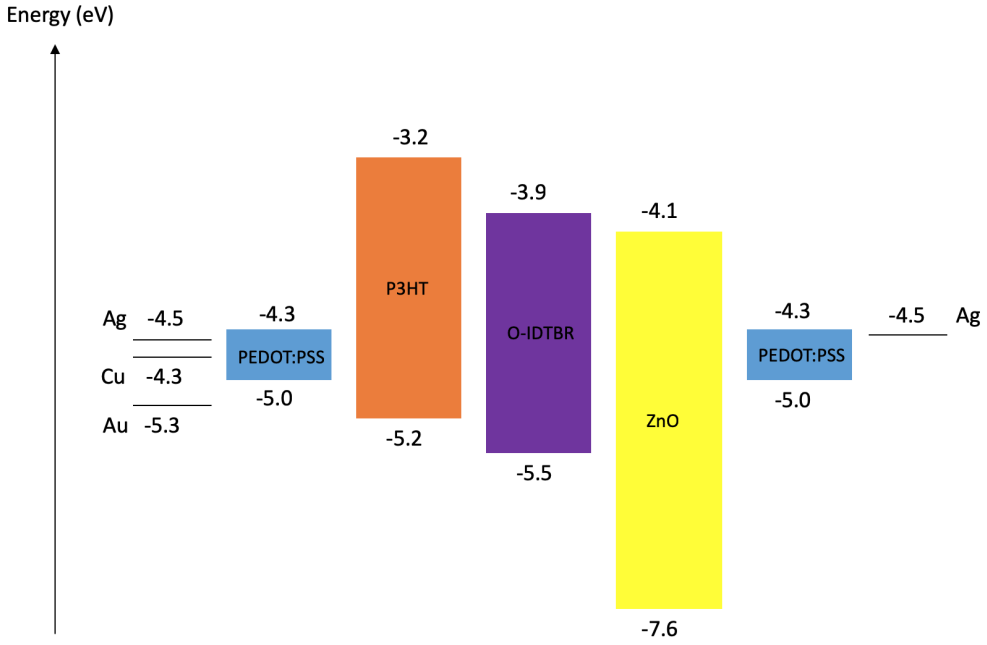

Figure 5.13. Energy levels of each material and possible electrodes

Devices with different areas

To finish the study, devices with larger areas were fabricated to demonstrate the scalability of this approach. Smaller area devices were measured by using shadow masks. The devices were made with both printed and evaporated silver electrodes. Table 5.7 summarizes the photovoltaic parameters obtained for different active area devices. The J-V curves are presented in figure 5.14.

Material	**Area** (cm^2)	**PCE (%)**	**FF (%)**	**Jsc** (**mA**/cm^2)	**Voc (V)**
Ag printed	4	2.31	54.04	5.84	0.733
	0.7	3.5	64.83	7.69	0.703
	0.25	3.58	67.25	7.9	0.674
	0.2	3.38	67.36	7.55	0.665
	0.08	2.98	62.59	7.55	0.632
Ag evap.	2.52	2.26	57.83	5.54	0.706
	0.7	3.72	62.68	8.41	0.705
	0.25	3.97	64.13	9.2	0.674
	0.2	3.73	64.69	8.69	0.665
	0.08	2.93	58.94	6.99	0.71

Table 5.7. PV parameters for different electrode materials

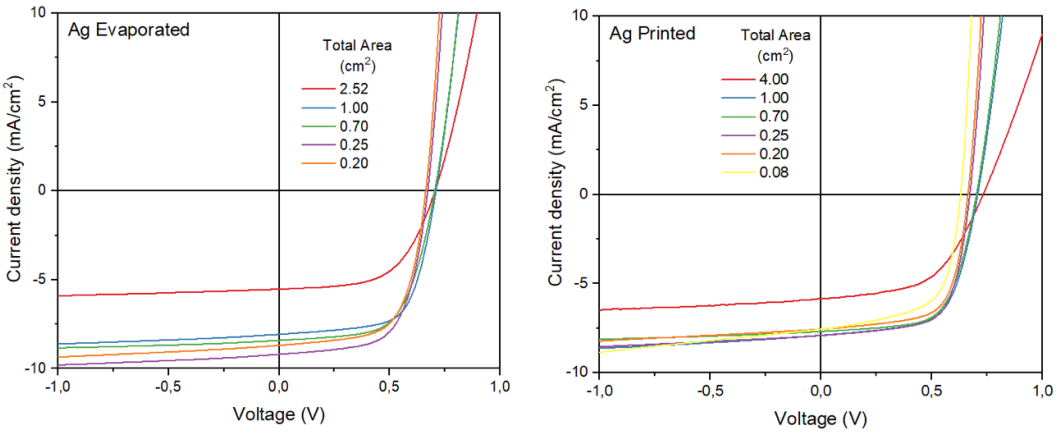

Figure 5.14. J-V curves of different area devices made with evaporated (left) and printed (right) silver electrodes

It can be seen that the $4cm^2$ yielded a PCE approximately 35% lower than that of our previous findings, as well as a much lower FF and Jsc. This is due to the series resistance R_s which increases with the area of the devices (Figure 5.15). The series resistance of the equivalent circuit of the solar cell (Figure 5.16) has been proven responsible for efficiency losses in upscaled devices [49].

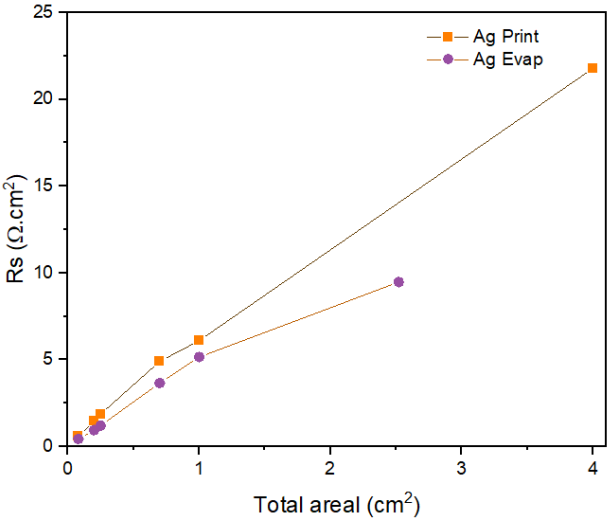

Figure 5.15. Series resistance for different active area devices

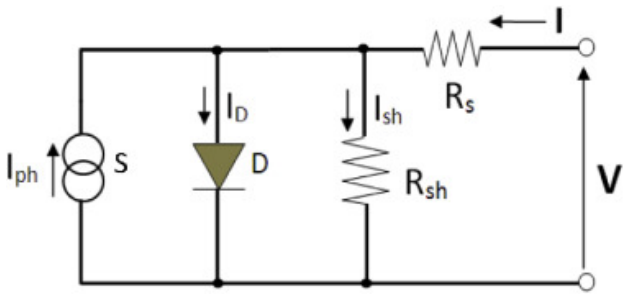

Figure 5.16. Equivalent circuit of an OPV

Chapter 6

Conclusions

This study provided an optimization approach for the fabrication of scalable, ITO and fullerene-free, flexible organic solar cells based on P3HT:O-IDTBR. The optimization procedure was centered around parameters, such as temperature and thickness, known to influence the performance of OSCs.
Our study allowed us to obtain state-of-the-art PCEs for organic solar cells using the system P3HT:O-IDTBR and silver electrodes, both including vacuum steps (evaporation) and under ambient conditions (flexographic printing). The champion devices obtained from this optimization procedure yielded PCEs of 3.80% and 3.59% respectively, the latter being the state-of-the-art efficiency for P3HT:O-IDTBR on an flexible, ITO-free substrate using roll-processing in open air.
This brings up an interesting point: printed silver devices are completely scalable and compatible with roll-to-roll technology, and have proven to be comparable in performance to evaporated silver cells. This means that a manufacturing tradeoff can be found, and vacuum steps are not absolutely necessary to improve the performance of NFA-based OPVs.

Additionally, this study proves that more research is to be done on the behaviour of metals as electrodes: it could be that the metal's work function and conductivity have a minor role compared to the actual interface between the metal and the underlying layer.

It has been demonstrated that non-fullerene acceptor-based devices can be successfully upscaled to working modules of few cm^2, and that an optimal fabrication can be carried out entirely using roll-to-roll equipment, with the option of including vacuum steps in the process or leaving them out.

This study confirms the adaptability of the system P3HT:O-IDTBR to large-scale manufacturing techniques, making it a worthy candidate for the steps towards commercialization.
This study would also like to underline the importance of directing research towards the scalability of non-fullerene systems in order to obtain PCEs corresponding to industrial-scale devices, and not laboratory scale ones.

Appendix A

Note: when saying "experiment", this implies the coating of an entire stripe with the specified conditions.

All of the experiments written below begin with positioning the flextrode onto the roll-coater and securing it with tape in a way that the two extremities are perfectly aligned.

Active layer

All the active layers mentioned in this study are followed by

- a butanol coating as surface treatment (drum speed of 1.2 ml/min, DT of 70°C, HT at RT and a flow rate of 0.25 ml/min)
- a coating of PEDOT:PSS as HTL (drum speed of 1.25 m/min, DT of 70°C, HT at RT and flow rate of 0.8 ml/min), dried for 45 minutes
- flexographic printing of the silver paste as electrodes with an area of 1 cm^2 (drum speed of 0.8 m/min, DT at 70°C), left to dry for 10 minutes
- encapsulation of the individual 1 cm^2 solar cells using a custom EPOXY glue cured under UV light for 3 minutes

in order to obtain functioning devices, which are what the "Results and discussion" chapter analyses.

Solution

The P3HT:O-IDTBR solution was obtained a 1:1 ratio of donor/acceptor. Other ratios were tested, such as 1:1.5 and 1.5:1, but did not yield better

results than the 1:1 solutions. 40 mg/mL of the 1:1 P3HT:O-IDTBR blend were then mixed with dichlorobenzene and 5% bromoanisole, then placed on a hot plate at 45°C with a magnetic stirrer for 15 minutes. The solution was left to cool down to room temperature before starting the experiments.

DT variations

For the drum temperature experiment, the coating head was left at room temperature, while the drum was heated to 50°C, 60°C, 70°C, 80°C, and 90°C, or left at room temperature, according to the experiment.
The solution was coated using the slot-die head with a drum speed of 0.6 m/min and a flow rate of 0.08 mL/min.

HT variations

Whilst keeping the drum temperature at 60°C, the slot-die coating head was heated using a thermistor, and the temperature was monitored with a thermocouple. Three experiments were performed, with temperatures of 40°C, 60°C and 80°C. Also in this case, the solution was coated using the hot slot-die head with a drum speed of 0.6 m/min and a flow rate of 0.08 mL/min.

Thickness variations

When matching the DT and HT to 60°C, a dry thickness of 480 nm was obtained, using the formula

$$d = \frac{cf}{\rho \nu w} \tag{6.1}$$

where d is the dry thickness of the film, c is the concentration of material in the solvent (here 40 mg/ml), w is the width of the coated stripe (here 1 cm), ρ is the density of the material (here 1.11 g/cm^3) and v is the drum speed. With the use of formula 6.1, three more thicknesses were tested: 360 nm, 600 nm and 720 nm with flow rates 0.06 ml/min, 0.10 ml/min and 0.12 ml/min respectively. The rest of the parameters remained unchanged.

HTL

All of the HTL variations are made on a 480 nm thick active layer stripe made with the conditions described in the previous section. The devices were finished with 250 nm of evaporated silver or flexographically printed silver, then encapsulated following the procedure described in the last section of this chapter.

Solutions

Pure PEDOT:PSS preparation

The pure PEDOT:PSS solution is prepared by sonication inside a Hielscher UIP1000hdT homogenizer. The resulting solution is then filtered with a 1 μm filter and is then ready for coating using an appropriate slot-die head with a larger hole due to its higher viscosity compared to the active layer solution.

Diluted PEDOT:PSS preparation

Three solutions of PEDOT:PSS diluted in IPA were prepared, with ratios IPA:PEDOT of 1:1, 2:1 and 3:1. This was done by measuring the volumes in syringes, then inserting both materials into a becker and stirring. The solutions were quickly used for coating in order to avoid phase separation as much as possible.

Coating variations

The pure PEDOT experiment was conducted in the same way as reported in the Active layer section above.
The 1:1 solution was coated with a flow rate of 0.625 ml/min, DT at 70°C, HT at RT, with a drum speed of 0.8m/min. A butanol surface treatment as described in the previous section was performed prior to this step.
The 2:1 solution was coated with a flow rate of 0.40 ml/min, DT at 70°C, HT at RT, with a drum speed of 0.8m/min. No butanol surface treatment was done.
Finally, the 3:1 solution was coated with a flow rate of 0.40 ml/min, DT at 70°C, HT at RT, with a drum speed of 0.8m/min. Again, no butanol surface treatment was done.

Electrodes

Flexographic printing of silver

A silver paste (DuPont 5025) was applied onto a flexographic printing roll, which was then fixed to the roll-coater. A drum speed of 0.8m/min and a DT of 70°C were used during this procedure. The roll was manually kept in contact with the underlying substrate. The resulting printed silver fingers were left to dry for 10 minutes, then the whole roll was removed from the mini roll-coater.

Thermal evaporations

The thermal evaporation procedure was the same for silver, gold, and copper electrodes. The metal beads were positioned in Tungsten boats and a pressure of 1.10^{-5} was kept during evaporation. The deposition rate of 5/s was monitored with an INFICON XTM/2 sensor. The layers had a thickness of 250 nm.

Encapsulation

Encapsulation was done by cutting the chosen amount of solar cells from the roll (1 for the optimization experiments, more for larger area devices), then sandwiching them between two glass slides with a drop of EPOXY-based glue (EPXR) on each side. The two slides were then pinched together and cured under UV light for 3 minutes, making sure that the side facing the light was not that of the PET substrate to avoid any influence on the device's performance.

Bibliography

[1] International Energy Agency. *IEA Data and statistics*.

[2] Bp. "Statistical Review of World Energy". In: (). URL: https://www.bp.com/en/global/corporate/energy-economics/statistical-review-of-world-energy/downloads.html.

[3] Nieves Espinosa et al. "Solar cells with one-day energy payback for the factories of the future". In: *Energy and Environmental Science* 5.1 (2012), pp. 5117–5132. ISSN: 17545692. DOI: 10.1039/c1ee02728j.

[4] Brian Azzopardi et al. "Economic assessment of solar electricity production from organic-based photovoltaic modules in a domestic environment". In: *Energy & Environmental Science* 4.10 (2011), p. 3741. ISSN: 1754-5692. DOI: 10.1039/c1ee01766g. URL: http://xlink.rsc.org/?DOI=c1ee01766g.

[5] H. Kallmann and M. Pope. *Photovoltaic effect in organic crystals*. 1959. DOI: 10.1063/1.1729992.

[6] A. Tsumura, H. Koezuka, and T. Ando. "Macromolecular electronic device: Field-effect transistor with a polythiophene thin film". In: *Applied Physics Letters* (1986). ISSN: 00036951. DOI: 10.1063/1.97417.

[7] Ossila. *Ossila website*. URL: https://www.ossila.com/pages/organic-photovoltaics-introduction.

[8] Yi Li et al. "Encapsulated Textile Organic Solar Cells Fabricated by Spray Coating". In: *ChemistrySelect* (2019). ISSN: 23656549. DOI: 10.1002/slct.201803929.

[9] Jong Su Yu et al. "Silver front electrode grids for ITO-free all printed polymer solar cells with embedded and raised topographies, prepared by thermal imprint, flexographic and inkjet roll-to-roll processes". In: *Nanoscale* (2012). ISSN: 20403372. DOI: 10.1039/c2nr31508d.

[10] ConditionalKO. *https://commons.wikimedia.org/w/index.phpcurid=39057566*. URL: https://commons.wikimedia.org/w/index.phpcurid=39057566.

[11] J Melskens et al. "Concepts and prospects of passivating contacts for crystalline silicon solar cells". In: *2015 IEEE 42nd Photovoltaic Specialist Conference (PVSC)*. 2015, pp. 1–6. ISBN: VO -. DOI: 10.1109/PVSC.2015.7355646.

[12] Riccardo Po et al. "Polymer- and carbon-based electrodes for polymer solar cells: Toward low-cost, continuous fabrication over large area". In: *Solar Energy Materials and Solar Cells* 100 (2012), pp. 97–114. ISSN: 09270248. DOI: 10.1016/j.solmat.2011.12.022. URL: http://dx.doi.org/10.1016/j.solmat.2011.12.022.

[13] Anders S Gertsen, Marcial Fernández, and Jens W Andreasen. "Scalable fabrication of organic solar cells based on non-fullerene acceptors - Accepted Manuscript". In: *Flexible and Printed Electronics* (2019).

[14] Mikkel Jørgensen et al. "Stability of polymer solar cells". In: *Advanced Materials* 24.5 (2012), pp. 580–612. ISSN: 09359648. DOI: 10.1002/adma.201104187.

[15] Www.laserfocusworld.com. "Air Mass". In: (). URL: https://www.laserfocusworld.com/lasers-sources/article/16566681/photovoltaics-measuring-the-sun.

[16] Wikipedia. *Solar simulator*.

[17] DTU. "Coursera - Introduction to solar cells". In: (). URL: https://www.coursera.org/learn/solar-cells/home/welcome.

[18] Lingxian Meng et al. "Organic and solution-processed tandem solar cells with 17.3% efficiency". In: *Science* (2018). ISSN: 10959203. DOI: 10.1126/science.aat2612.

[19] Shigehiko Mori et al. "Organic photovoltaic module development with inverted device structure". In: *Materials Research Society Symposium Proceedings*. 2015. ISBN: 9781510806177. DOI: 10.1557/opl.2015.540.

[20] Jon E. Carlé et al. *Overcoming the Scaling Lag for Polymer Solar Cells*. 2017. DOI: 10.1016/j.joule.2017.08.002.

[21] Riccardo Po et al. *From lab to fab: How must the polymer solar cell materials design change?-an industrial perspective*. 2014. DOI: 10.1039/c3ee43460e.

[22] Roar Søndergaard et al. “Roll-to-roll fabrication of polymer solar cells”. In: *Materials Today* 15.1-2 (2012), pp. 36–49. ISSN: 13697021. DOI: 10.1016/S1369-7021(12)70019-6.

[23] L. Wengeler et al. “Investigations on knife and slot die coating and processing of polymer nanoparticle films for hybrid polymer solar cells”. In: *Chemical Engineering and Processing: Process Intensification* (2011). ISSN: 02552701. DOI: 10.1016/j.cep.2010.11.002.

[24] S. Strohm et al. “P3HT: Non-fullerene acceptor based large area, semi-transparent PV modules with power conversion efficiencies of 5%, processed by industrially scalable methods”. In: *Energy and Environmental Science* 11.8 (2018), pp. 2225–2234. ISSN: 17545706. DOI: 10.1039/c8ee01150h.

[25] Seyeong Song et al. “Hot slot die coating for additive-free fabrication of high performance roll-to-roll processed polymer solar cells”. In: *Energy and Environmental Science* 11.11 (2018), pp. 3248–3255. ISSN: 17545706. DOI: 10.1039/c8ee02221f.

[26] Seok In Na et al. “High Performance Roll-to-Roll Produced Fullerene-Free Organic Photovoltaic Devices via Temperature-Controlled Slot Die Coating”. In: *Advanced Functional Materials* 29.6 (2019), pp. 1–10. ISSN: 16163028. DOI: 10.1002/adfm.201805825.

[27] C. Kapnopoulos et al. “Gravure Printed Organic Photovoltaic Modules Onto Flexible Substrates Consisting of a P3HT: PCBM Photoactive Blend”. In: *Materials Today: Proceedings*. 2016. DOI: 10.1016/j.matpr.2016.02.006.

[28] Matthieu Manceau et al. “Effects of long-term UVvisible light irradiation in the absence of oxygen on P3HT and P3HT: PCBM blend”. In: *Solar Energy Materials and Solar Cells* (2010). ISSN: 09270248. DOI: 10.1016/j.solmat.2010.03.012.

[29] Frederik C. Krebs. *Fabrication and processing of polymer solar cells: A review of printing and coating techniques*. 2009. DOI: 10.1016/j.solmat.2008.10.004.

[30] Elodie Destouesse Madsen et al. “Slot-die processing and encapsulation of non-fullerene based ITO-free organic solar cells and modules”. In: *Flexible and Printed Electronics* (2019). ISSN: 2058-8585.

[31] V. A. Trukhanov and D. Yu Paraschuk. “Non-fullerene acceptors for organic solar cells”. In: *Polymer Science - Series C* (2014). ISSN: 1555614X. DOI: 10.1134/S181123821401010X.

[32] Leiping Duan et al. "Progress in non-fullerene acceptor based organic solar cells". In: *Solar Energy Materials and Solar Cells* 193.November 2018 (2019), pp. 22–65. ISSN: 09270248. DOI: 10.1016/j.solmat.2018.12.033. URL: https://doi.org/10.1016/j.solmat.2018.12.033.

[33] Andreas Distler et al. "The effect of PCBM dimerization on the performance of bulk heterojunction solar cells". In: *Advanced Energy Materials* 4.1 (2014), pp. 1–6. ISSN: 16146832. DOI: 10.1002/aenm.201300693.

[34] Baobing Fan et al. "Achieving over 16% efficiency for single-junction organic solar cells". In: *Science China Chemistry* (2019). ISSN: 18691870. DOI: 10.1007/s11426-019-9457-5.

[35] Minh Trung Dang, Lionel Hirsch, and Guillaume Wantz. "P3HT:PCBM, best seller in polymer photovoltaic research". In: *Advanced Materials* (2011). ISSN: 09359648. DOI: 10.1002/adma.201100792.

[36] Cara J. Mulligan et al. "A projection of commercial-scale organic photovoltaic module costs". In: *Solar Energy Materials and Solar Cells* (2014). ISSN: 09270248. DOI: 10.1016/j.solmat.2013.07.041.

[37] Mikkel Jørgensen et al. *Stability of polymer solar cells*. 2012. DOI: 10.1002/adma.201104187.

[38] Kim Tremel and Sabine Ludwigs. *P3HT Revisited – From Molecular Scale to Solar Cell Devices*. 2014. ISBN: 978-3-662-45144-1. DOI: 10.1007/978-3-662-45145-8.

[39] Andrew Wadsworth et al. "Progress in Poly (3-Hexylthiophene) Organic Solar Cells and the Influence of Its Molecular Weight on Device Performance". In: *Advanced Energy Materials* 8.28 (2018), pp. 1–15. ISSN: 16146840. DOI: 10.1002/aenm.201801001.

[40] Sarah Holliday et al. "High-efficiency and air-stable P3HT-based polymer solar cells with a new non-fullerene acceptor". In: *Nature Communications* 7 (2016), pp. 1–11. ISSN: 20411723. DOI: 10.1038/ncomms11585.

[41] Kjell Cnops et al. "Energy Level Tuning of Non-Fullerene Acceptors in Organic Solar Cells". In: *Journal of the American Chemical Society* (2015). ISSN: 15205126. DOI: 10.1021/jacs.5b02808.

[42] Kuan Liu et al. "Roll-coating fabrication of flexible organic solar cells: Comparison of fullerene and fullerene-free systems". In: *Journal of Materials Chemistry A* (2016). ISSN: 20507496. DOI: 10.1039/c5ta07357j.

[43] Xi Fan et al. "PEDOT:PSS for Flexible and Stretchable Electronics: Modifications, Strategies, and Applications". In: *Advanced Science* 6.19 (2019). ISSN: 21983844. DOI: 10.1002/advs.201900813.

[44] Safa Shoaee, Martin Stolterfoht, and Dieter Neher. "The Role of Mobility on Charge Generation, Recombination, and Extraction in Polymer-Based Solar Cells". In: *Advanced Energy Materials* 8.28 (Oct. 2018), p. 1703355. ISSN: 1614-6832. DOI: 10.1002/aenm.201703355.

[45] Yun Hui L. Lin, Michael A. Fusella, and Barry P. Rand. "The Impact of Local Morphology on Organic Donor/Acceptor Charge Transfer States". In: *Advanced Energy Materials* 8.28 (2018), pp. 1–16. ISSN: 16146840. DOI: 10.1002/aenm.201702816.

[46] Fuwen Zhao, Chunru Wang, and Xiaowei Zhan. "Morphology Control in Organic Solar Cells". In: *Advanced Energy Materials* 8.28 (2018), pp. 1–34. ISSN: 16146840. DOI: 10.1002/aenm.201703147.

[47] Said Karim Shah et al. "Optimization of active-layer thickness, top electrode and annealing temperature for polymeric solar cells". In: *AIMS Materials Science* (2017). ISSN: 23720468. DOI: 10.3934/matersci.2017.3.789.

[48] Yuming Wang et al. "Optical Gaps of Organic Solar Cells as a Reference for Comparing Voltage Losses". In: *Advanced Energy Materials* 8.28 (2018), pp. 1–10. ISSN: 16146840. DOI: 10.1002/aenm.201801352.

[49] Jonathan D. Servaites et al. "Efficiency enhancement in organic photovoltaic cells: Consequences of optimizing series resistance". In: *Advanced Functional Materials* (2010). ISSN: 1616301X. DOI: 10.1002/adfm.200901107.